

Large Airfoil Models

Howon Lee ^{*}, Pranay Seshadri [†], and Juergen Rauleder[‡]
Georgia Institute of Technology, Atlanta, Georgia, 30322

Large language models (LLMs) are rapidly transforming the way people are learning and understanding complex topics. Their capability to be fine-tuned to answer questions on specialized topics suggests the viability of a “large airfoil model (LAM),” which can answer complex technical questions on airfoil aerodynamics. Such a model requires a rich historical dataset it can easily access. For gaps within the database, the model must be able to generate physic-based responses. We present the main components of the LAM: (1) an airfoil surface pressure information repository of experiments (ASPIRE), a database of digitized pressure measurements sourced from publicly available experimental reports, and (2) a deep airfoil prediction tool (ADAPT), capable of predicting airfoil C_p distributions and integrated force and moment coefficients, including their uncertainties. ADAPT employs deep kernel learning, which performs Gaussian Process Regression in a ten-dimensional latent space learned by a neural network; crucially, it incorporates the reported experimental uncertainties for inference. Exemplary results for three airfoils are shown. The model accurately predicts the C_p distribution and the aerodynamic coefficients under varied flow conditions. The predicted C_p on the test data yields a mean absolute error in enclosed area (MAE_{enclosed}) of 0.029.

Nomenclature

ADAPT	=	A Deep Airfoil Prediction Tool
ASPIRE	=	Airfoil Surface Pressure Information Repository of Experiments
c	=	chord length [m]
c_d	=	sectional drag coefficient
c_l	=	sectional lift coefficient
c_m	=	sectional moment coefficient
C_p	=	sectional pressure coefficient
LAM	=	Large Airfoil Model

^{*}Graduate Research Assistant, Daniel Guggenheim School of Aerospace Engineering, hlee981@gatech.edu

[†]Associate Professor, Daniel Guggenheim School of Aerospace Engineering, prse@gatech.edu.

[‡]Assistant Professor, Daniel Guggenheim School of Aerospace Engineering, juergen.rauleder@gatech.edu, Associate Fellow AIAA

M	=	freestream Mach number
x/c	=	non-dimensional chordwise location
α	=	angle of attack [degrees]
μ	=	mean
σ^2, σ	=	variance, standard deviation

I. Introduction

Large language models (LLMs) such as ChatGPT [1], Claude [2], and Gemini [3], are now at the forefront of artificial intelligence, rapidly gaining popularity as they make learning and understanding complex topics more accessible. Beyond general-purpose LLMs, it is also possible to create specialized models, designed to answer questions and provide insights on specific topics or datasets [4–6].

In the context of aerodynamics, there are several key questions that aerodynamicists may ask themselves during the wing (fixed-wing, rotary-wing, or wind turbine) design process: What is the maximum lift coefficient? Does stall occur at the leading or trailing edge? How do drag and stall behavior change with Mach number? Is there a significant pitching moment? These questions inherently involve operations on sectional pressure coefficients, C_p . This motivates the idea that a LLM for airfoil aerodynamics, or a *large airfoil model* (LAM), could be used to answer these queries. To accurately respond to user inquiries, the LAM must be able to (1) obtain information by leveraging historical data, or (2) in lieu of available data, generate its own C_p distributions and perform the necessary operations to obtain chosen quantities of interest (QoIs).

As a first step in the development of the LAM, it is necessary to design a means to predict aerodynamic properties of airfoils, a requirement ubiquitous across fixed wings, rotorcraft, and turbomachinery. Traditionally, airfoil properties have been obtained by wind tunnel experiments or computational fluid dynamics (CFD) simulations. With recent developments in computational power and data-driven modeling, there have been efforts to map airfoil geometric information to its C_p directly using machine learning (ML). For example, Yilmaz and German [7] applied a classification framework to develop a convolutional neural network (CNN) trained on airfoil pressures obtained from a panel method code. The model successfully predicted the pressure distribution as a series of discretized C_p values. Hui et al. [8] proposed a five-layer CNN model to predict airfoil C_p , trained from their in-house airfoil database of RANS simulations. Zhang [9] utilized a variational autoencoder on a RANS dataset, where an encoder was used to extract latent features of the database of varying airfoil geometries, angles of attack (α), and freestream Mach numbers (M). A decoder was then used to reconstruct the C_p within this latent space. Intrinsically, these models aim to find a latent variable representation.

An alternate approach is to explicitly employ dimensionality reduction techniques; active subspaces [10] and related methods have had tremendous success in identifying subspaces for QoIs derived from C_p distributions. Active spaces

were successfully used to map airfoil geometries and operating conditions to low-dimensional embeddings that capture the parameters' relations to lift and drag [11]. The orthogonal complement of the *active subspace*, termed the *inactive subspace* can prove useful for identifying insensitivities and robustness. Wong et al. [12] showed that samples from the inactive subspace could be used to ascertain whether a compressor blade with manufacturing variations or degradation could provide near identical performance to nominal. This answer to how “forgiving” an airfoil is to imperfections is a crucial component in robust aerodynamic design. Wong et al. [13] proposed employing embedded ridge approximations to find the dimension-reducing subspace based on an underlying pressure field around an airfoil.

There have also been multiple efforts to develop models that predict sectional lift, drag, and moment coefficients (c_l , c_d , and c_m). For example, Zhang et al. [14] predicted XFOIL-based c_l and c_d using deep learning methodologies such as CNNs and multi-layered perceptrons (MLP). Liu et al. [15] coupled a CNN with Bayesian optimization to predict the aerodynamic coefficients obtained from OpeanFOAM simulations. Cornelius and Schmitz [16] adopted a feed-forward neural network trained on an extensive database of OVERFLOW simulations named PALMO. However, these models treat each QoI independently, rather than taking advantage of the fact that C_p inherently is related to the coefficients. Building a model that is capable of leveraging the underlying physics would enjoy the added benefit of improved interpretability. For instance, one would be able to identify leading/trailing edge stall and reattachment, which translates pitch link loads, a critical element in rotor design.

A drawback found in some of the aforementioned approaches is the lack of a framework to characterize uncertainty. While it is not yet common to identify and rigorously propagate uncertainties into integrated metrics during design processes, incorporating uncertainty quantification techniques will be a crucial step towards making aviation much safer. Sources of uncertainty in airfoil data include the difference between theoretical and actual airfoil geometry, unsteadiness in the freestream, and unsteadiness introduced by flow separation. Neural networks, deterministic in nature, have difficulty quantifying such uncertainties. One way to develop an uncertainty-aware model is to take a Bayesian approach. For example, Anhichem et al., used Gaussian Process (GP) regression to build surrogate models for pressure distributions over an OAT15A airfoil [17] and a RBC12 half-wing-fuselage multi-fidelity model [18] via data fusion.

From the survey of previous works, it becomes evident that existing ML models are dependent on an extensive sweep of CFD simulations for training. This is due to the fact that experimental data, the *ground truth*, are much more limited in accessibility. The architecture of certain neural networks, such as CNN, also require C_p values along a preset grid, which makes them unsuitable for training on data sourced from different experiments. Furthermore, the sole reliance on CFD may introduce numerical biases due to the researcher's modeling decisions, such as the choice of turbulence models. We can thus summarize the limitations in existing literature of ML airfoil prediction tools as the following:

- reliance on a particular CFD simulation to build a training database, which may be prone to numerical biases,
- minimal leveraging of physical relationships between C_p and aerodynamic coefficients, and
- limited framework to characterize and propagate uncertainties associated with the training data and the model.

We now turn to the other requirement for a robust LAM—a rich historical database. Several open-source databases exist to train or tweak LLMs [19–21]. There have also been datasets created to fine-tune existing LLMs for more aerospace applications, such as `aeroBERT-NER` [6] which was used to adapt the BERT language model to identify named entities in aerospace requirements. However, we also make the observation that the vast, nearly century-old historical repository of experimental airfoil pressure data is left untapped by the wider aerospace community. This is because, while many reports and papers are available in NASA Technical Reports Server (NTRS) or Aerospace Research Central (ARC), the majority of the data is locked away in images or in poorly legible bulk scans. Digitizing the publicly available data into an accessible, open-source database is thus a paramount and time-critical task, as in a few decades, the next generation may be unaware of the existence of this wealth of experimental data.

Building this database would also be pivotal in creating a ML model that can overcome existing limitations. Ideally, a probabilistic ML model would be able to capture and propagate experimental uncertainty when predicting C_p and the related c_l , c_d , and c_m for an airfoil under specific M and α . Such a model will be free of numerical biases from CFD simulations, and can be used to supplement existing databases with C_p predictions for untested operating conditions.

In this paper, we present the primary components of the Large Airfoil Model*, the airfoil surface pressure information repository of experiments (ASPIRE) and a deep airfoil prediction tool (ADAPT). ADAPT employs a deep kernel learning architecture, combining deep learning for latent space identification and a probabilistic method for uncertainty characterization. The input features of the model are designed to incorporate the unstructured (relative to CFD) experimental data from ASPIRE, a digitized database of historical C_p measurements. Figure 1 shows the workflow of the model. While only a forward problem is presented in the paper, the proposed components will eventually be used for other tasks, including inverse problems. The complete model, which will be coupled with a LLM, will allow users to perform a variety of aerodynamic tasks based on the design questions that an aerospace engineer would ask, rather than requiring the explicit technical inputs. Aspirationally, this represents a transformative shift in how aerodynamicists engage with data and models, paving the way for a more intuitive and innovative approach to aerodynamic design.

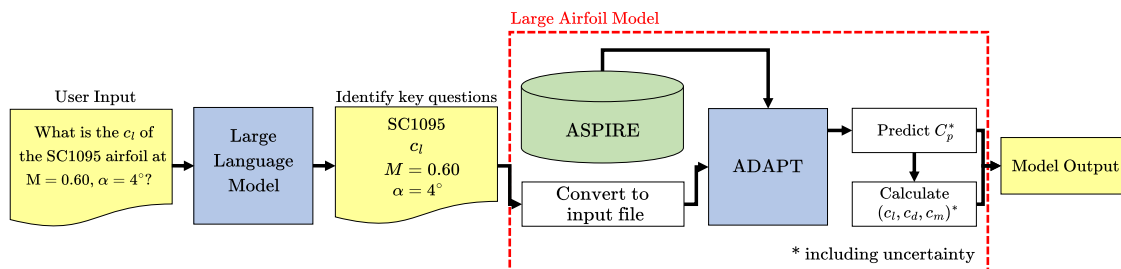


Fig. 1 Flowchart depicting the proposed forward problem workflow. The LAM proposed in this paper is wrapped in red.

*Accessible online on <https://large-airfoil-model.azurewebsites.net>

The paper is organized as follows. In Section II, ASPIRE is introduced. The methodology and challenges of the data digitization process are detailed, followed by a description of the range of available data. In Section III, ADAPT, a novel deep probabilistic model to predict airfoil C_p based on experimental training data, is proposed. The accuracy and computational efficiency of the model’s prediction of surface pressures and aerodynamic coefficients is assessed in Section IV.

II. Airfoil Surface Pressure Information Repository of Experiments

A. Data Mining

A data mining campaign was undertaken to create a digital database of *strictly experimental* pressure distributions for numerous airfoils. This database, ASPIRE, consists of experimental C_p measurements for various airfoil geometries at different angles of attack, chord-based Reynolds numbers, and freestream Mach numbers. The test articles of these experiments are of an *infinite wing* configuration as seen in Fig. 2, where the wing spans throughout the entire wind tunnel test section to minimize three-dimensional effects. ASPIRE’s data sources include government reports, technical notes, theses, and published papers.



Fig. 2 “Infinite wing” test articles for wind tunnel experiments. From left to right: Refs. [22, 23, 24]

In each source, the pressure distribution data was reported in either a tabulated or graphical format. This data was then digitized as a comma separated values (CSV) file. For tabulated results, the data was digitized using an online optical character recognition (OCR) tool called ExtractTables [25], followed by manual proofreading to correct any inaccuracies. The conversion accuracy depended heavily on the legibility of the original document. Due to the early publication dates of many technical reports, the quality of PDF files were often poor. Examples of the varying legibility from different documents can be inferred from Fig. 3. In some cases, it was difficult to accurately identify experimental values. If an entry was considered unreliable, its value was determined indirectly by comparing it to the plotted results (if available), estimating based on the authors’ best knowledge of airfoil C_p trends, or omitting the data point.

If presented in a graphical format with no accompanying tabulated results, the data was digitized using WebPlotDigitizer [34]. This online tool enables manual extraction of individual data points. However, extracting certain points,

1.177 1.066 -.939 -.862 -.411 -.396 -.921 -.390 -.401 -.353 -.387 -.280	1.181 -.967 -.799 -.676 -.946 -.919 -.904 -.394 -.984 -.333 -.366 -.297	1.187 -.846 -.773 -.753 -.310 -.300 -.285 -.314 -.363 -.314 -.343 -.227	X/C CP ML UPPER SURFACE 0.0 0.7343 0.4223 0.0130 -0.5057 0.9785 0.0440 -0.1889 0.8412 0.1040 -0.1491 0.8243 0.1640 -0.7798 1.1035 0.2480 -0.7161 1.0727 0.3300 -0.8561 1.1401 0.4100 -0.7009 1.0661 0.5770 -0.4114 0.9763 0.7300 -0.3025 0.9894 0.9000 -0.2394 0.8624 1.0000 -0.1413 0.8202 LOWER SURFACE 0.0 0.7343 0.4223 0.0160 0.9806 0.2640 0.0440 0.6154 0.4845 0.1040 0.5950 0.4948	X/C CP P/L/PT ML/C UPPER SURFACE 0.0000 1.1041 1.0012 0.0000 0.112 -2.030 0.4141 0.8833 0.239 -5.562 0.3141 1.0240 0.379 -8.779 0.173 1.1920 0.503 -8.041 0.184 1.1608 0.637 -9.718 0.106 1.2043 0.793 -9.009 0.139 1.1981 0.901 -9.281 0.094 1.2006 1.000 -8.778 0.395 1.2327 1.000 -8.714 0.398 1.2342 1.001 -8.678 0.395 1.2309 1.002 -8.640 0.213 1.1762 1.002 -9.281 0.208 1.1806 1.002 -9.227 0.398 1.2262 1.003 -1.0104 0.385 1.2221 1.000 -7.7608 0.502 1.1221 1.000 -8.208 0.524 0.820 1.002 -3.140 0.527 0.912 1.002 -1.290 0.350 0.829 1.001 -0.268 0.640 0.7886	X/C CP X/C CP UPPER SURFACE LOWER SURFACE 0.0000 1.0498 0.040 0.620 0.0020 -0.0428 0.100 0.4172 0.0200 -1.4012 0.0200 0.1752 0.0300 -1.2324 0.0300 0.0866 0.0500 -0.9981 0.0500 -0.013 0.0700 -0.8742 0.0700 -0.0575 0.1000 -0.7242 0.1000 -0.0936 0.1500 -0.6883 0.1500 -0.1215 0.2000 -0.5816 0.2000 -0.0942 0.2500 -0.5341 0.2500 -0.0922 0.3000 -0.5160 0.3000 -0.0804 0.3500 -0.4755 0.3500 -0.0744 0.4000 -0.4571 0.4000 -0.0842 0.4500 -0.4530 0.4500 -0.0804 0.5000 -0.4548 0.5000 -0.1100 0.5500 -0.4556 0.5500 -0.1304 0.6000 -0.4615 0.6000 -0.1129 0.6500 -0.4781 0.6500 0.0209 0.7000 -0.4969 0.7000 0.2492 0.7500 -0.5120 0.7500 0.3423 0.8000 -0.5190 0.8000 0.4067 0.8500 -0.5042 0.8500 0.4514 0.9000 -0.4497 0.9000 0.4796 0.9300 -0.3391 0.9300 0.4770					
.253 .261 .280 .278 .294	.384 .851 .375 .417 .483	.888 .416 .464 .497 .587	X/C CP 0 0.31 0.41 0.51 0.56 0.60 0 -1.72 -1.48 -0.95 -0.71 -0.49 .006 -2.05 -2.92 -2.57 -2.96 -2.40 .016 -1.49 -1.67 -2.05 -2.26 -2.37 .027 -1.11 -1.20 -1.38 -1.56 -1.81 .051 -0.89 -0.96 -1.03 -1.14 -1.22 .080 -0.67 -0.72 -0.75 -0.81 -0.83 0.106 -0.62 -0.66 -0.69 -0.72 -0.76 0.134 -0.50 -0.52 -0.55 -0.57 -0.58 0.159 -0.44 -0.47 -0.49 -0.51 -0.52 0.235 -0.39 -0.42 -0.43 -0.45 -0.46 0.305 -0.37 -0.39 -0.40 -0.42 -0.43 0.351 -0.34 -0.36 -0.36 -0.38 -0.39 0.399 -0.32 -0.35 -0.35 -0.37 -0.38 0.448 -0.29 -0.32 -0.32 -0.34 -0.36 0.502 -0.25 -0.28 -0.28 -0.29 -0.30 0.551 -0.22 -0.26 -0.24 -0.25 -0.24 0.600 -0.18 -0.20 -0.20 -0.21 -0.21 0.655 -0.15 -0.16 -0.16 -0.16 -0.16 0.758 -0.11 -0.11 -0.11 -0.11 -0.10 0.804 -0.06 -0.07 -0.06 -0.06 -0.06 0.904 0.02 0.01 0.02 0.01 0.02 0.955 0.03 0.03 0.04 0.04 0.05 1.000 0.29 0.18 0.14 0.11 0.12	X/C CP P/L/PT ML/C UPPER SURFACE 0.0000 1.1110 0.9941 0.0021 0.112 -0.6024 0.8986 0.7604 0.233 -0.4491 0.959 0.8924 0.379 -0.606 0.559 0.9597 0.503 -0.573 0.529 0.9449 0.637 -0.5038 0.386 0.9187 0.793 -0.536 0.387 0.9187 0.901 -0.593 0.308 0.9340 1.000 -0.592 0.301 0.9340 1.001 -0.577 0.307 0.9307 1.002 -0.5627 0.308 0.9382 1.002 -0.5715 0.307 0.9440 1.002 -0.5813 0.302 0.9457 0.940 -0.5764 0.304 0.9421 0.863 -0.5371 0.333 0.8279 0.730 -0.472 0.387 0.9031 0.502 -0.3939 0.410 0.9709 0.332 -0.1906 0.620 0.7401 0.211 -0.6271 0.846 0.7481	.828 .878 .440 .554 .716	.497 .588 .675 .797 .927	.610 .718 .818 .819 .902	.894 1.000 .903 .198 -.891	.992 .870 .221 -1.265 -2.815	.919 .595 -1.502 -2.500 -4.203

Fig. 3 Varying document legibility encountered during data mining. From left to right, top row: Refs. [26, 27, 28, 29], bottom row: Refs. [30, 31, 32, 33].

particularly those at near the leading and trailing edges, proved challenging as the C_p values converge. This issue was especially pronounced in graphs where multiple pressure distributions were plotted on the same axes. Figure 4 illustrates an example of such difficult cases. In these instances, the data points were carefully obtained by zooming in or by the authors' informed estimates based on airfoil physics. If neither method was viable, the point was omitted.

In many sources, experimental accuracy was noted by the authors. These were often reported as a single scalar value in terms of the maximum magnitude of the error, or the maximum percentage error. In ASPIRE, these values were recorded in an accompanying tag file. Additionally, if the uncertainties in the independent variables such as those of the freestream Mach number, angles of attack, or pressure sensor locations were found in source documents, they were also recorded. An example of a tag file included in the database can be seen in Fig. 5.

B. Available Data

At the time of publishing, ASPIRE consists of 2802 unique pressure distributions from 68 airfoils taken across various airfoil families and applications. All profiles of the airfoils included in the database, compared against the commonly studied NACA 0012, is shown in Fig. 6. Airfoil profiles thicker than a NACA 0012 at the given chordwise location are colored in varying shades of red. Profiles thinner than the NACA 0012 are colored in shades of blue.

The available data ranges from -30° to 30° in angles of attack (α) and 0.0 to 1.0 in freestream Mach number (M).

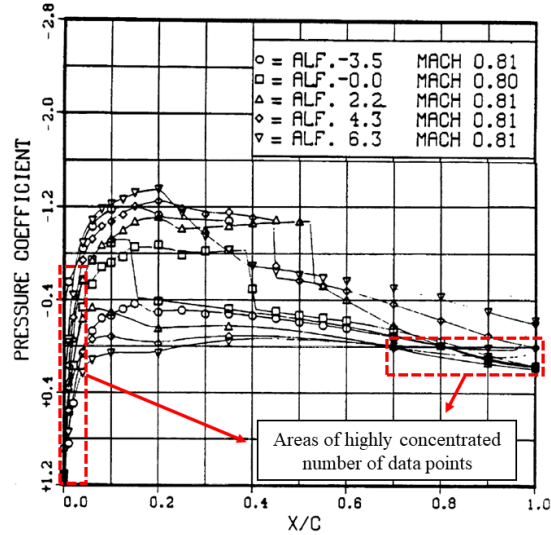


Fig. 4 Areas of highly concentrated data points typically found in airfoil pressure distribution plots. Original graph from [35].

```

1  {
2    "flow_conditions" : { Wind tunnel conditions
3      "reynolds" : "1.85e6 - 4.0e6", Reynolds number, provided or calculated
4      "mach" : "0.3 - 0.83", Freestream Mach number, provided or calculated
5      "freestream" : "", Freestream velocity [m/s], provided or calculated
6      "alpha": "0, 2, 3, 4, 6, 8" Geometric angles of attack [deg]
7    },
8    "uncertainty" : { Experimental uncertainties, 1σ unless stated otherwise
9      "x" : "", Uncertainty in pressure orifice location [x/c]
10     "cp" : "0.005 + 0.01|Cp|", Uncertainty in pressure coefficient
11     "alpha": "0.04", Uncertainty in angle of attack [deg]
12     "mach": "0.003" Uncertainty in Mach number
13   },
14   "airfoil": { Airfoil information
15     "name": "NACA 0012", Airfoil name
16     "camber": "N", Is the airfoil cambered? "Y" or "N"
17     "supercritical": "N", Is the airfoil supercritical? "Y" or "N"
18     "application": "General" Airfoil applications: "General", "Rotor", "Wind Tunnel", etc.
19   },
20   "source": { Source material
21     "name": "AGARD-AR-138", Source name
22     "year": "1979", Year of publication
23     "page": "A1-A13", Pages of where the data was presented
24     "type": "tabulated", Original data format: "graph", "tabulated", etc.
25     "url": "https://www.sto.nato.int/publications/AGARD/AGARD-AR-138/AGARD-AR-138.pdf" URL of source PDF file
26   },
27   "meta" : { Information related to data digitization
28     "num_cases": "19", Number of digitized pressure distributions
29     "num_remaining": "", If not finished, how many remain?
30     "notes": "" Any points of note
31   }
32 }

```

Fig. 5 An example ASPIRE tag file for a NACA 0012; experimental data from [36].

This includes the incompressible, transonic and sonic regimes. The distribution of available C_p data at a given operating condition is shown in Fig. 7. The color and the number in the center plot denotes the number of unique airfoils available for a given M - α combination. Marginal histograms are plotted to provide a clear visualization of the available data at

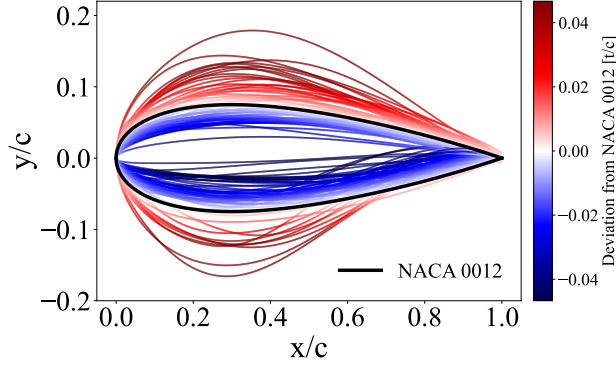


Fig. 6 Geometric profiles of airfoils in the database, colored by thickness compared to the baseline NACA 0012

specific α or M . The data distribution is presented in terms of airfoil families, design usage, and supercriticality.

It is evident from the data distribution plots that there is a wide variety of airfoil families and applications. It can also be observed that the available experimental data is mostly concentrated around $\alpha = -4.0^\circ - 12.0^\circ$ and $M = 0.3 - 0.9$. This is attributable to the fact that airfoils for general aviation or rotor applications are operated in the compressible regime, resulting in an experimental focus on the higher freestream Mach numbers. For a similar reason, we see that the wind turbine airfoil experiments are concentrated at lower M . Extreme angles of attack, both positive and negative, are not explored thoroughly in experimental literature, explaining the dearth of data at $\alpha \leq -4.0^\circ$ or $\alpha \geq 12.0^\circ$.

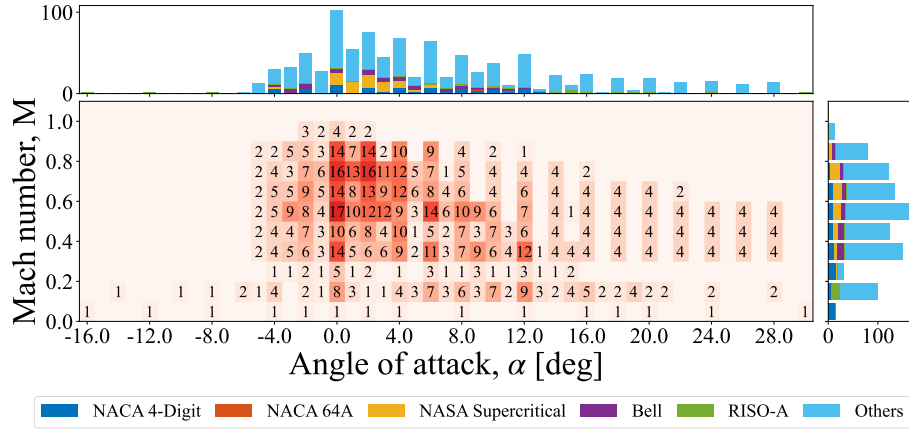
By releasing the database as a publicly available repository, we aim to continue expanding the database and fill in any gaps existing in terms of airfoil families and years of publication through contributions from the aerospace community. The distribution of digitized and not yet digitized data can be seen in Fig. 8.

C. Data Pre-processing

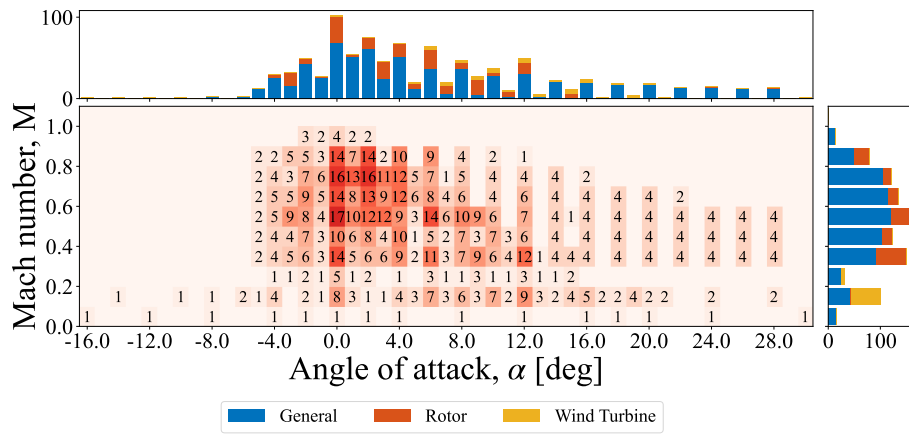
In many experimental reports, C_p is plotted with respect to the normalized coordinates in the chordwise direction, x/c . The coordinate system spans from 0 to 1, where 0 corresponds to the leading edge and 1 to the trailing edge. Such a coordinate system does not permit one to distinguish between the airfoil's upper and lower surfaces. Since a model trained on the dataset should adhere to the true *physical* behavior of airfoils, it is necessary that the pressures at the leading and trailing edges match. In other words, the periodicity at the boundaries must be maintained.

To address this, a conformal mapping-based approach was adopted; the normalized airfoil chordwise location is transformed into two variables: \hat{x} and \hat{y} in a polar coordinate system. In this procedure, $x/c = \{x \in \mathbb{R} | 0 \leq x \leq 1\}$ is transformed to $\hat{x} = \{x \in \mathbb{R} | -1 \leq x \leq 1\}$, corresponding to the x -value of the equivalent unit circle. The equivalent angle is obtained via: $\theta = \cos^{-1}(x/c)$, implying $\hat{y} = \sin \theta$, where $\hat{y} = \{y \in \mathbb{R} | -1 \leq y \leq 1\}$ is the y -value of the unit circle. The transformation is visualized in Fig. 9, where it is evident that the sign of \hat{y} corresponds to the upper and lower surfaces. At the leading and trailing edges, $\hat{y} = 0$, which enforces periodicity.

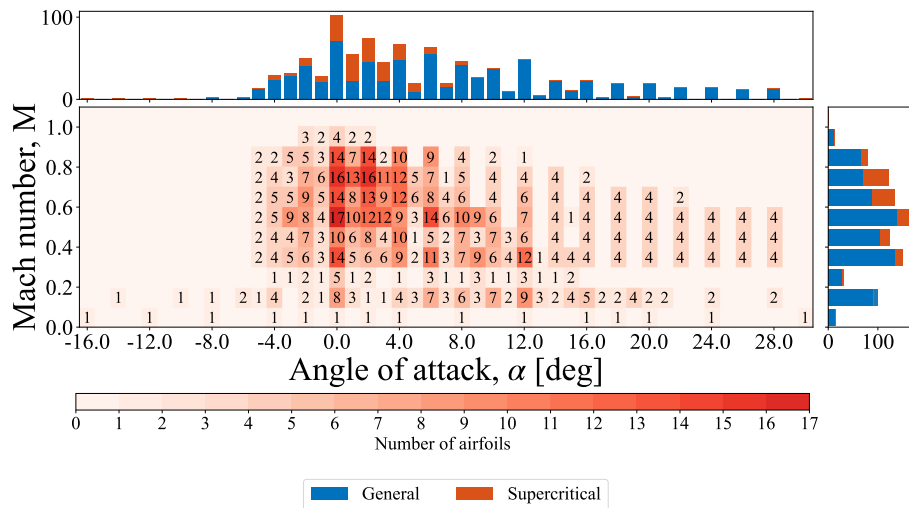
The input data matrix for ADAPT was created by down-selecting the data in ASPIRE such that $-4.0^\circ \leq \alpha \leq 12.0^\circ$



(a) Distribution of available airfoil pressure data and the marginal histograms categorized by airfoil family



(b) Distribution of available airfoil pressure data and the marginal histograms categorized by airfoil usage



(c) Distribution of available airfoil pressure data and the marginal histograms categorized by airfoil supercriticality

Fig. 7 The distribution of available C_p data in terms of the number of unique airfoils at each freestream Mach number and angles of attack. The marginal histograms are organized by different categories.

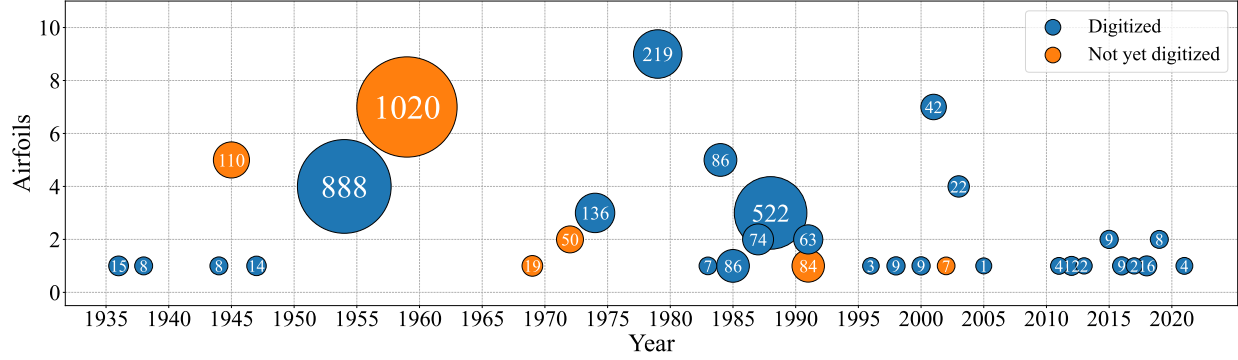


Fig. 8 Bubble plot of data that has and has not been digitized. The number on each circle represents the number of unique pressure distributions available within the source material.

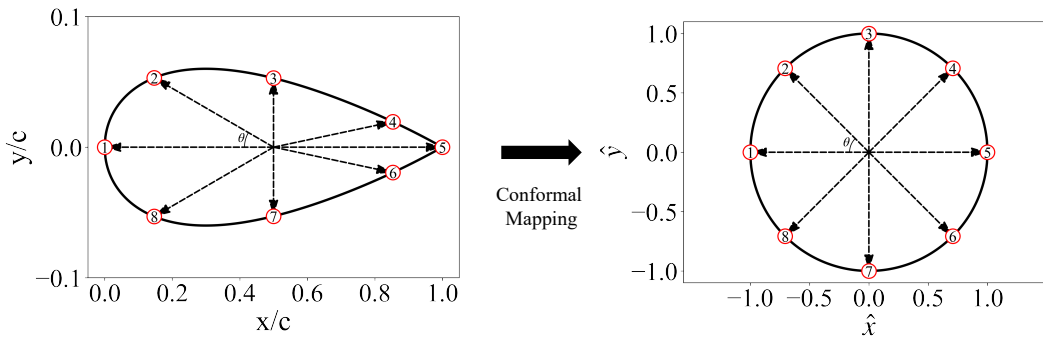


Fig. 9 Transformation of airfoil coordinates $(x/c, y/c)$ to polar coordinates (\hat{x}, \hat{y}) via conformal mapping

and $0.0 \leq M \leq 0.75$. These ranges for α and M were chosen due to the abundance of data available within them. Additionally, only data points with a chord-based Reynolds number (Re) on the order of 10^6 were included. Fixing the Re helped to eliminate Reynolds number effects and reduce the dimensionality of the data. A Reynolds number on the order of 10^6 was chosen because, in this regime, the viscous effects of the freestream are considered minimal compared to the inertial effects [37]. In order to eliminate inconsistencies with the boundary layer transition behavior, data sets where the boundary layer was artificially tripped were excluded. The data entries were then pre-processed to extract key feature vectors (i.e. input variables) necessary for the model to predict the pressure distributions. The input variables for the model were: 28 y -values of the airfoil geometry at set chordwise locations for upper and lower surfaces respectively, the freestream Mach number, the angle of attack, \hat{x} , and \hat{y} . This corresponded to a total of 60 input variables.

III. A Deep Airfoil Prediction Tool

As discussed in Sec. I, using experimental data instead of simulations allows us to benefit from the quantified measurement uncertainties reported in many experimental studies. Additionally, the approach helps us avoid potential biases associated with choosing a specific simulation tool—such as RANS with a particular turbulence model, which may not be suitable for all flow regimes—or relying on a set of tools with varying levels of fidelity.

A. Machine Learning Model

ADAPT is deep kernel learning model, inspired by the modeling framework introduced by Wilson et al., 2013 [38]. In ADAPT, a Gaussian process model is applied to the final hidden layer of a neural network, conditioned on the output observations of C_p . This approach allows us to construct kernels that capture the expressive power of deep neural network architectures. At its core, ADAPT is a Bayesian method, resulting in a multivariate Gaussian distribution over the space of C_p values. This can be written as

$$C_p \left(\underbrace{\alpha, M}_{\text{operating conditions}}, \underbrace{\mathbf{x}/c, \mathbf{y}/c}_{\text{geometry}}, \underbrace{\hat{x}, \hat{y}}_{\text{coordinates}} \right) \equiv C_p \left(\underbrace{\mathbf{u}}_{\text{all inputs}} \right) \sim \mathcal{N}(\mu(\mathbf{z}, \mathbf{t}), \Sigma(\mathbf{z}, \mathbf{t})), \quad (1)$$

where $\underbrace{\mathbf{z}}_{\text{latent variable}} = \underbrace{f_{\mathbf{w}}(\mathbf{u})}_{\text{deep neural network with weights } \mathbf{w}},$

where the notation $f_{\mathbf{w}} : \mathbf{u} \rightarrow \mathbf{z}$ denotes the deep neural network that is parameterized with weights \mathbf{w} , where $\mathbf{u} \in \mathbb{R}^d$ comprises the operating conditions, geometry and specific *conformal* airfoil coordinates, i.e., $\mathbf{u} = \{\alpha, M, \mathbf{x}/c, \mathbf{y}/c, \hat{x}, \hat{y}\}$. The outputs of the deep neural network are latent variables $\mathbf{z} \in \mathbb{R}^s$. In this latent space, we build the Gaussian process model that is fully specified by a mean and covariance function. The covariance function is based on a two-point kernel function $k_{\mathbf{t}}(\mathbf{z}, \mathbf{z}')$, where the subscript \mathbf{t} indicates certain hyperparameters that are used to parameterize the kernel function. The overall structure of the model is presented in Fig. 10. It is important to note that the number of discrete locations at which C_p may be evaluated can be tailored by the user after training, making this functional form more advantageous than many deep neural networks that utilize a pre-defined fixed discretization for the output.

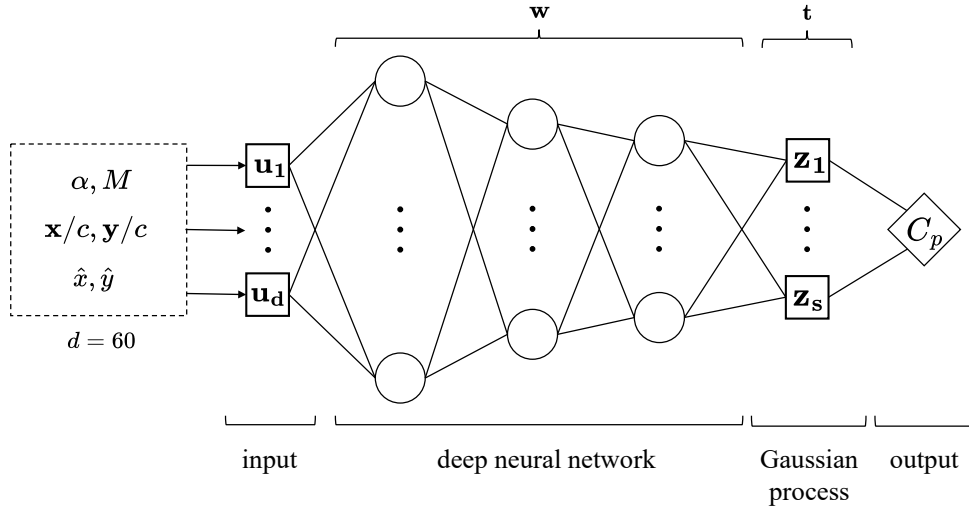


Fig. 10 Overview of the deep kernel learning model that maps a 60-dimensional training input to a 10-dimensional active space which is used to predict C_p distributions.

In ADAPT, a fully connected neural network (FCNN) with a [60-1000-1000-500-50-10] architecture is used to map from the space of inputs \mathbf{u} to the space of latent variables \mathbf{z} . The number of input variables is $d = 60$ and the number of latent variables, which is driven by the network architecture, is $s = 10$. For the Gaussian process layer, we use a Matérn 5/2 kernel function. The choice allows us to more accurately capture aerodynamic phenomena on airfoils such as rapid pressure changes at the suction peak, transition from laminar to turbulent boundary layer, and compressibility/shock effects—all of which lead to large derivatives in C_p . Further details on the network architecture and Gaussian process model are provided in Appendices A–C.

As with most Bayesian frameworks, ADAPT requires the user to define the likelihood (i.e., the noise model). To this end, we first provide fixed noise values for each pressure measurements based on the reported accuracy of the original experiments. If the source material did not quantify the uncertainty of its measurements, the standard deviation was assumed to be 0.01, which was approximately the order of magnitude in errors observed in many sources. Some additional noise was also inferred to account for the human error introduced during the digitization process outlined in Sec. II.A. It was found that the additional noise resulted in improved numerical stability of the predictions.

B. Model Training

The data was split into a training set and a test set, used to train the model and assess model accuracy, respectively. The sets were partitioned with respect to airfoils as opposed to withholding a certain percentage of available C_p . This ensured that the predictions are performed on airfoils unseen by the model. Experimental measurements of three airfoils were selected as the test set: SC1095 [35], NASA Supercritical Airfoil 9a [29], and NACA 63-415 [39]. The selections covered all applications within ASPIRE (general aviation, rotor, wind turbine) and supercriticality. In total, 40416 C_p data points were utilized to train the model and 879 data points were reserved for testing.

The training was performed on an NVIDIA A100 GPU. The Adam optimizer [40] was used to maximize the model’s marginal likelihood, which served as the loss function, given the training data. The optimizer had an initial learning rate of 1.0×10^{-3} , with a step decay of 0.5 every 1000 epochs, resulting in a learning rate of 1.0×10^{-4} after 3000 epochs of training. Beyond that point, the learning rate was set to decay linearly between 1.0×10^{-3} and 1.0×10^{-4} over 200-epoch cycles, for a total of 2000 additional epochs. Stochastic Weight Averaging (SWA), which involves equally averaging the weights traversed by the optimizer, was performed by restoring the best weights for each cycle. As reported by Refs. [41] and [42], we found that the SWA procedure improved generalization of the LAM.

The mean absolute error in the area enclosed by the predicted C_p curves ($\text{MAE}_{\text{enclosed}}$) was found to be 0.033. We report the model accuracy in terms of $\text{MAE}_{\text{enclosed}}$ due to the fact that mean absolute error (MAE) or the mean absolute percentage error (MAPE) of C_p can be misleading. When using MAE, even slight misalignment between predicted and actual C_p values across the entire airfoil can result in consistently large absolute errors, exaggerating the overall error metric. In the case of MAPE, small absolute errors can result in extremely high percentage errors when the true value is

near zero, which occurs commonly in C_p . $\text{MAE}_{\text{enclosed}}$ avoids the limitations while remaining intuitive, since the error in the area enclosed by the pressure curves is analogous to an error in c_l .

The model was trained via an exact GP inference, where the covariance matrix of the training set is directly inverted. The operation was bottle-necked by the high memory requirement and high computational complexity. To accommodate the continuous expansion of ASPIRE, it is essential to enhance the model’s ability to handle larger datasets. Approximate methods, such as stochastic variational inference [43] and inducing point methods [44], offer potential solutions. However, our findings indicate that these approaches result in considerably reduced accuracy, with only marginal improvements observed from increasing the number of inducing points. With 1000 inducing points, the $\text{MAE}_{\text{enclosed}}$ was 0.148, an order of magnitude greater than that of the exact method. Increasing the number to 10,000 yielded in approximately the same error. As the model is fully open-source, we encourage contributions from the community to address this issue.

C. Model Limitations

The main limitation of LAM is the same as that of most other ML models; for inputs beyond the range of the training data, the predictions become significantly less reliable. Therefore, it is necessary to keep in mind how the training data is distributed. For example, predictions for a wind turbine airfoil would be less reliable at higher freestream Mach numbers compared to results in the incompressible regime due to the relative lack of available training data.

In the user input, the airfoil thickness locations (\mathbf{x}/c) are fixed. With only 60 discrete chordwise locations, it can be challenging to accurately model small geometric features. As a result, the model cannot capture the effects of subtle variations in geometry, such as small cavities in the trailing edge and surface roughness, both of which can influence aerodynamic performance. The model is thus best suited for predictions on smooth airfoils.

Lastly, the model is more memory intensive than traditional neural networks. The GP element of ADAPT requires the model to store the full covariance matrix of the training data of size $40,416 \times 40,416$. The model thus requires more overhead memory compared to neural networks which only require the storage of the weights and biases of each layer. Reduction of required memory could be achieved via low-rank approximation of the covariance matrix using techniques such as singular value decomposition. Exploration of different methods are attractive subjects for future study.

IV. Results and Discussion

A. Pressure Distributions

To initially assess the capability of the LAM, a random subset of the training data was selected and input into the model. The predicted mean C_p and 2 standard deviations are displayed in Fig. 11. The plots showcase the LAM’s capability to fit the training data, which is important as the ADAPT evaluations at the training data point need not necessarily interpolate the training data. Moreover, it can be seen that the 95% confidence intervals of predicted pressure

distributions differ significantly for each airfoil. Regions of higher uncertainty exist for cases where the noise reported by the source material is inherently high (e.g. the NACA 0012 airfoil), or for cases where the amount of training data is sparse (e.g. negative angles of attack as seen on NASA LS(1)-0013 and OLS/TAAT cases). A significant increase in the uncertainty also occurs on regions of pronounced shock effects, as seen on the suction side of the MBB-A3 at $M = 0.70$.

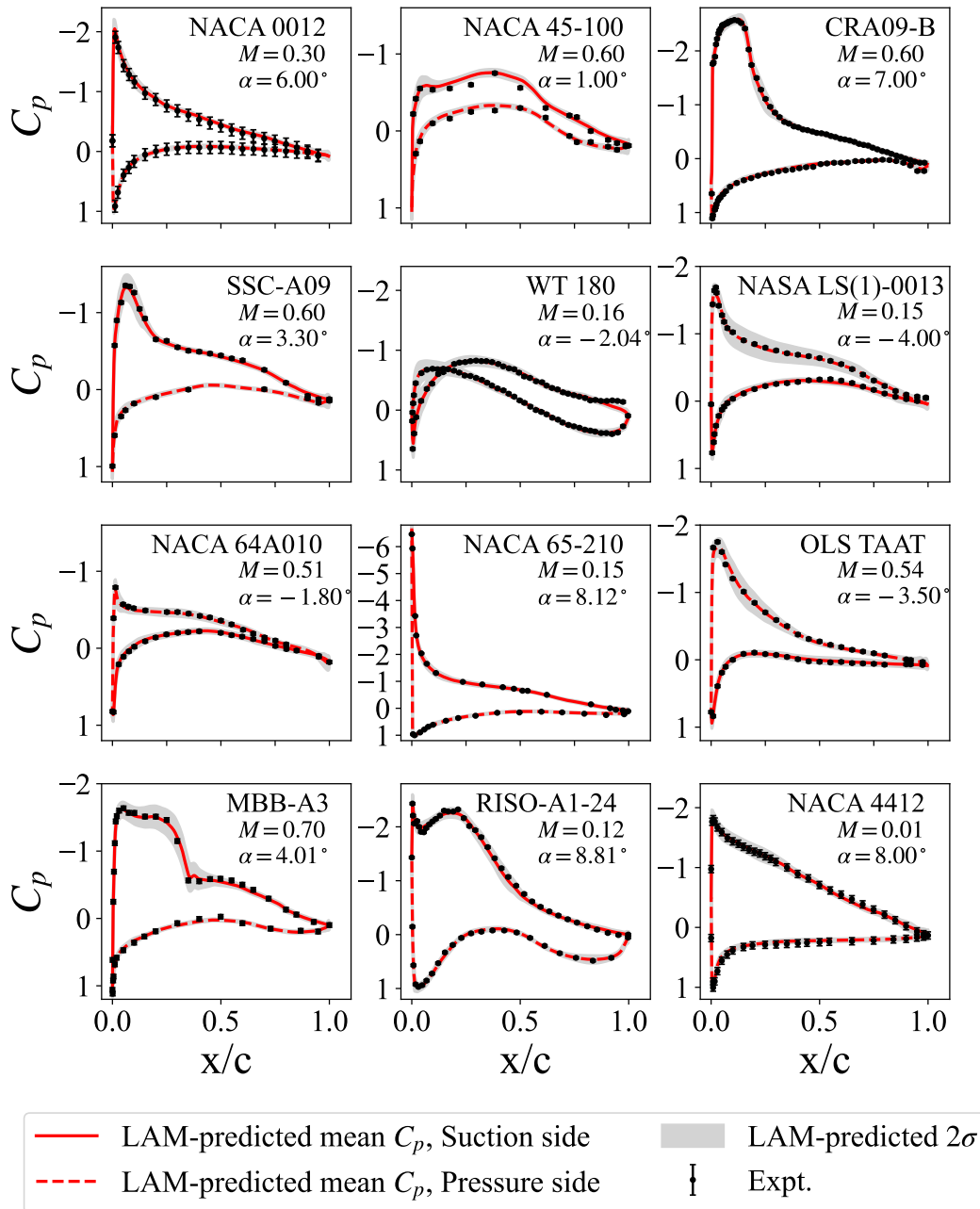


Fig. 11 Predicted C_p for the training set. The error bars represent two standard deviations.

It is also worth noting from Fig. 12 that, with the conformal transformation during data pre-processing (Sec. II.C), the C_p at the upper and lower surfaces of the trailing edge match. In contrast, it is clearly seen that a model trained on

the one-dimensional input x/c yields a pressure mismatch at the trailing edge, which is a non-physical behavior.

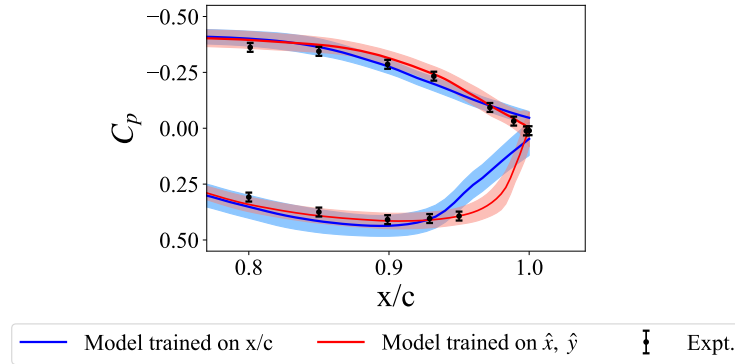


Fig. 12 Zoom view of a trailing edge C_p and two standard deviations, predicted from models trained on normalized airfoil chordwise location (blue) and conformal coordinates (red).

The remaining figures represent the predictions on the test set, airfoils previously unseen by the model. Figure 13 shows the predicted C_p for the SC1095 airfoil, designed for rotorcraft applications. We observe good agreement between the predictions and the test data overall, with a $\text{MAE}_{\text{enclosed}}$ of 0.027 for the data subset. We especially note the model’s capability to accurately capture compressibility effects for $\alpha \geq 6.1^\circ$ when transitioning from $M = 0.40$ to 0.60. The model also predicts the onset of stall, as the change in the pressure distribution is minimal when increasing the angle of attack beyond $\alpha = 9.0^\circ$. While some inaccuracies in the mean C_p can be observed for negative angles of attack, the experimental measurements fall within the 95% confidence interval of the predictions.

The predicted C_p and the corresponding uncertainty for the Supercritical Airfoil 9a is presented in Fig. 14. The $\text{MAE}_{\text{enclosed}}$ for the airfoil was found to be 0.018. Surface pressures of this supercritical airfoil are significantly “flatter” on the suction side compared to those of conventional airfoils. The agreement between the predictions and the experimental data suggests that the model accurately captures the aerodynamic characteristics associated with supercritical geometries. Furthermore, the model is able to accurately predict the onset of shock on the airfoil, as indicated by the rapid change in the pressure observed in the $M = 0.70$ cases (bottom row). The locations of shock formation are often very sensitive to various factors such as the surface roughness of the test article or chord-based Reynolds number. This inherent uncertainty is captured by the model through an increase in the confidence interval.

Lastly, Fig. 15 shows the model outputs for the NACA 63-415, typically used for wind turbines. The $\text{MAE}_{\text{enclosed}}$ between the predictions and the experimental data from the test set was found to be 0.041. From the figure, it can be confirmed that the model adequately predicts the distinct C_p around the airfoil, which changes much more gradually than that of the other two airfoils. However, there are some regions of noticeable underprediction at the suction peak. This is most notable at $\alpha = 4.0^\circ$ and 12.0° . This contributes to the higher $\text{MAE}_{\text{enclosed}}$ compared to the other two airfoils. The lower accuracy can be attributed to the relatively smaller size of wind turbine airfoil data.

In summary, all presented results clearly indicate that the LAM performs well on both training and test sets. The

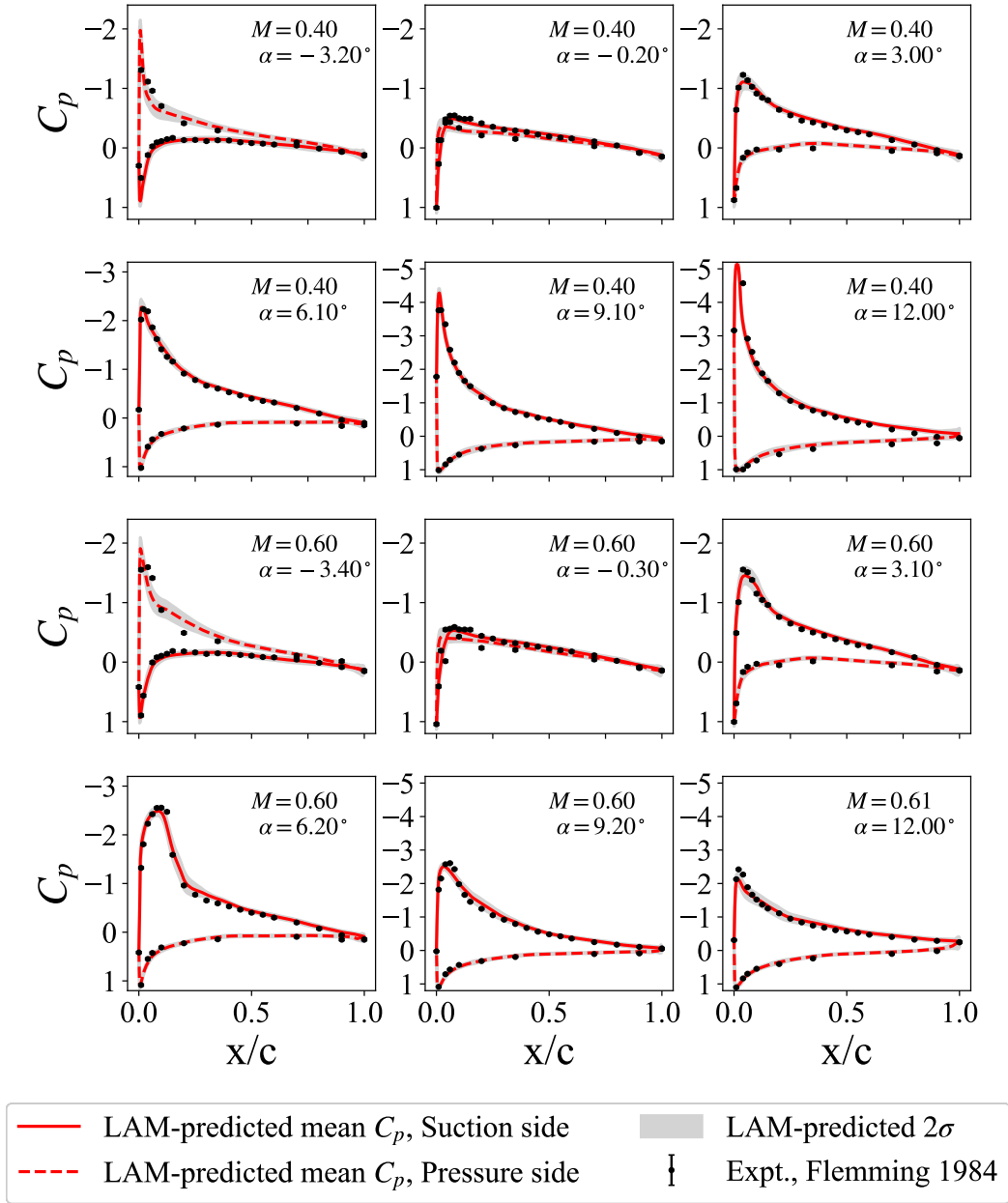


Fig. 13 SC1095: Predicted C_p under various M and α . The error bars represent two standard deviations.

model has the ability to generalize well to different airfoil families optimized for varying aerodynamic applications, while accurately capturing their unique behaviors. The strong generalization capability arises from the fact that different airfoil families occupy separate regions within the model’s active space. Interested readers are encouraged to refer to Appendix D for a basic analysis of ADAPT’s latent variables.

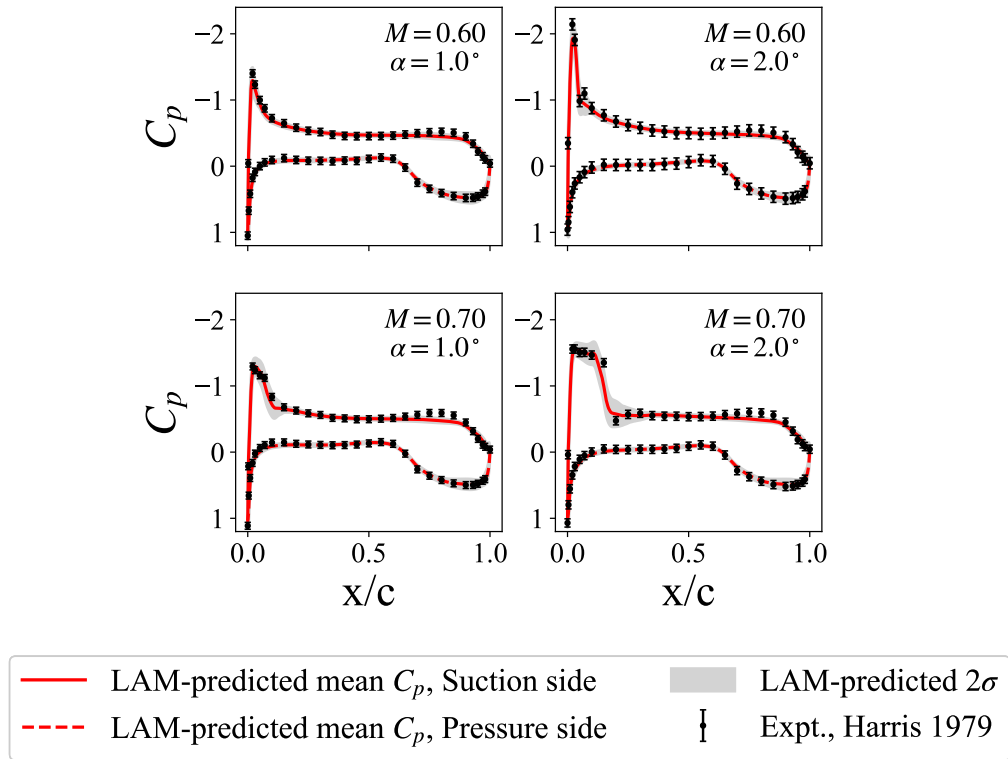


Fig. 14 NASA Supercritical Airfoil 9a: Predicted C_p under various M and α . The error bars represent two standard deviations.

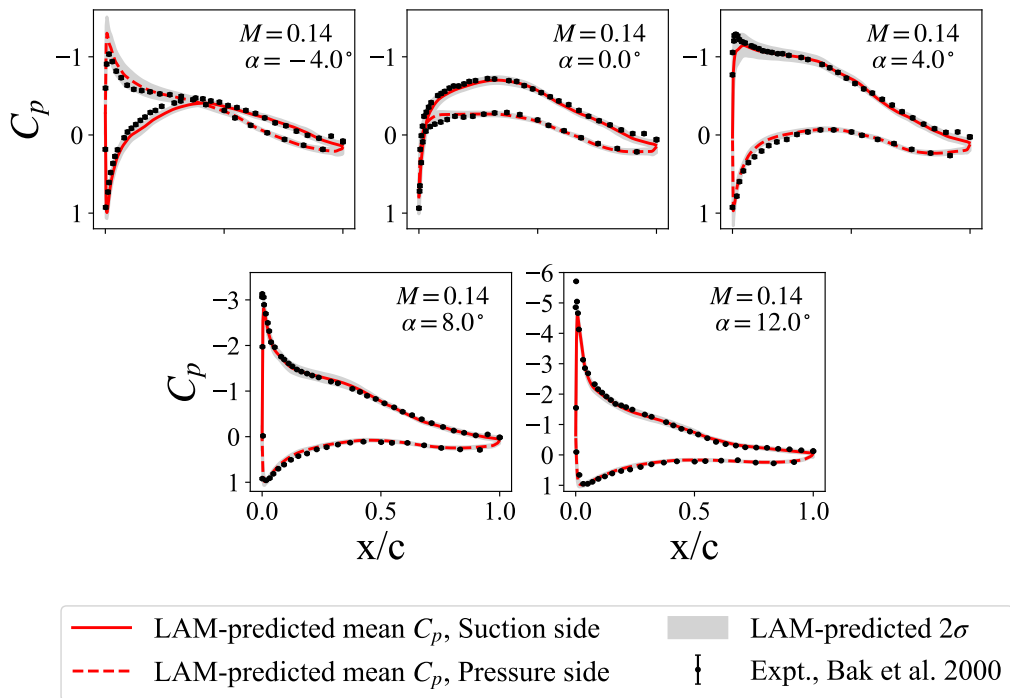


Fig. 15 NACA 63-415: Predicted C_p under various M and α . The error bars represent two standard deviations.

B. Aerodynamic Force Coefficients

The normal, axial, and moment coefficients about the quarter-chord for a two-dimensional body are defined below:

$$c_n = \int_0^1 \left(C_{p,l} \left(\frac{x}{c} \right) - C_{p,u} \left(\frac{x}{c} \right) \right) d\frac{x}{c} + \int_0^1 \left(c_{f,u} \frac{d(y_u/c)}{d(x/c)} + c_{f,l} \frac{d(y_l/c)}{d(x/c)} \right) d\frac{x}{c}, \quad (2)$$

$$c_a = \int_0^1 \left(C_{p,u} \left(\frac{x}{c} \right) \frac{d(y_u/c)}{d(x/c)} - C_{p,l} \left(\frac{x}{c} \right) \frac{d(y_l/c)}{d(x/c)} \right) d\frac{x}{c} + \int_0^1 (c_{f,u} + c_{f,l}) d\frac{x}{c}, \quad (3)$$

$$\begin{aligned} c_m = & \int_0^1 \left[\left(C_{p,l} \left(\frac{x}{c} \right) - C_{p,u} \left(\frac{x}{c} \right) \right) \left(\frac{x}{c} - \frac{1}{4} \right) \right] d\frac{x}{c} \\ & - \int_0^1 \left(c_{f,u} \frac{d(y_u/c)}{d(x/c)} - c_{f,l} \frac{d(y_l/c)}{d(x/c)} \right) \left(\frac{x}{c} - \frac{1}{4} \right) d\frac{x}{c} \\ & + \int_0^1 \left(C_{p,u} \left(\frac{x}{c} \right) \frac{d(y_u/c)}{d(x/c)} + c_{f,u} \right) \frac{y_u}{c} d\frac{x}{c} \\ & + \int_0^1 \left(-C_{p,l} \left(\frac{x}{c} \right) \frac{d(y_l/c)}{d(x/c)} + c_{f,l} \right) \frac{y_l}{c} d\frac{x}{c} \end{aligned} \quad (4)$$

where c_f is the skin friction coefficient, α is the angle of attack, and the subscripts u and l denote quantities of interest on upper and lower surfaces respectively. Here, C_p is a function of the normalized chordwise location, $\frac{x}{c}$.

In ADAPT, C_p is a Gaussian process; for a given set of inputs, the deep neural network projects \mathbf{u} to the latent space \mathbf{z} , where C_p has a mean and covariance defined over the conformal domain, as defined in Sec. II.C. If one introduces the assumption that contributions of skin friction are negligible—valid in most non-zero angles of attack and at higher M [45]—then, c_l , c_d and c_m can be approximate as

$$c_n \approx \frac{1}{2} \int_{-1}^1 (C_{p,l}(\hat{x}) - C_{p,u}(\hat{x})) d\hat{x}, \quad (5)$$

$$c_a \approx \frac{1}{2} \int_{-1}^1 \left(C_{p,u}(\hat{x}) \frac{d(y_u/c)}{d(x/c)} - C_{p,l}(\hat{x}) \frac{d(y_l/c)}{d(x/c)} \right) d\hat{x}, \quad (6)$$

$$\begin{aligned} c_m \approx & \frac{1}{2} \left\{ \int_{-1}^1 (C_{p,l}(\hat{x}) - C_{p,u}(\hat{x})) \left(\hat{x} + \frac{1}{2} \right) d\hat{x} \right. \\ & + \int_{-1}^1 \left(C_{p,u}(\hat{x}) \frac{d(y_u/c)}{d(x/c)} \frac{y_u}{c} \right) d\hat{x} \\ & \left. - \int_{-1}^1 \left(C_{p,l}(\hat{x}) \frac{d(y_l/c)}{d(x/c)} \frac{y_l}{c} \right) d\hat{x} \right\}, \end{aligned} \quad (7)$$

$$c_l = c_n \cos \alpha - c_a \sin \alpha, \quad (8)$$

$$c_d = c_n \sin \alpha + c_a \cos \alpha, \quad (9)$$

where $C_{p,u}(\hat{x})$ and $C_{p,l}(\hat{x})$ are model-predicted pressure coefficients with respect to the x -location in *conformal coordinates*. The bounds of the integral differ from Eqs. 2–4 due to the change of coordinate systems.

The above quantities are linear operators acting on a Gaussian process; therefore, they must also be Gaussian [46].

However, because the inputs are passed through a deep neural network, a series of non-linear operations, it is not possible to express the posterior distribution of the aerodynamic quantities analytically. They must be obtained by performing the integral numerically instead. We approach this problem using the Monte Carlo method.

To begin, we generate 10,000 samples from the multivariate normal distribution associated with C_p , which was deemed sufficient for convergence. Each sample is pushed through Eqs. 5–9 to obtain c_l , c_d , and c_m . From the integrated samples, the mean and the standard deviation of the aerodynamic coefficients are calculated. The overall workflow is captured in Fig. 16.

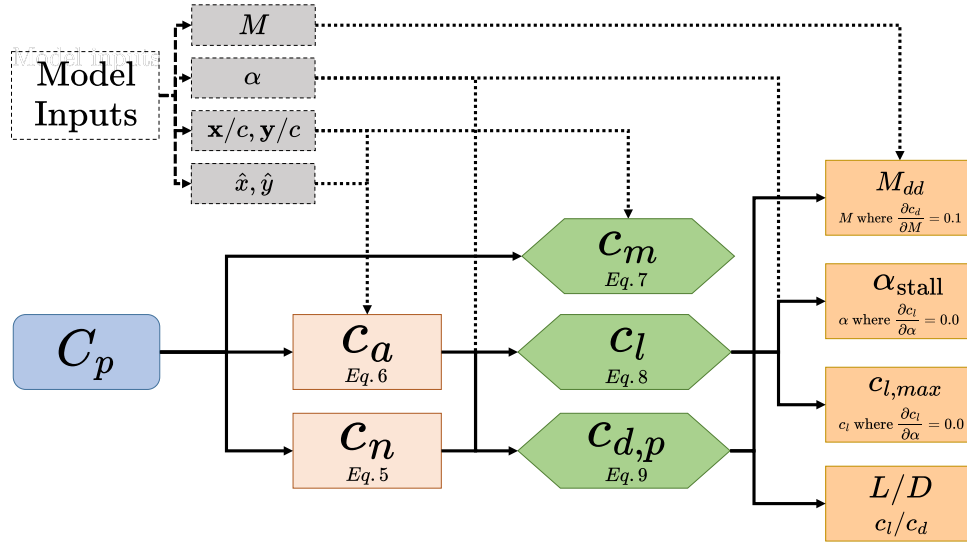


Fig. 16 Workflow of obtaining key aerodynamic quantities of interest of an airfoil based on model output C_p . While we limit our investigation to the green blocks in this paper, more intermediate design parameters in orange can be obtained similarly.

Figure 17 shows the predicted sectional lift coefficients. Overall, good correlation between the predictions and the experimental measurements can be observed. Figures 17a and 17b show that the lift curve slope increases and $c_{l,max}$ decreases with increasing freestream Mach number. These trends, in agreement with the experimental data points, is the expected behavior of airfoils [37]. We also confirm accurate predictions of stall, with the lift curve slope approaching zero at higher α . However, it was found that there was some underprediction of c_l in Fig. 17b at $M = 0.70$ although the experimental data points are near the 95% confidence interval. The error between the predicted mean and measurement was greatest at $\alpha = 2.5^\circ$ where $\Delta c_l = 0.05$. The discrepancy can be attributed to the fact that the model predicts a slightly earlier onset of shock as observed in Fig. 14.

In Fig. 18, we highlight the comparison between the predicted and experimentally measured c_d for the SC1095 airfoil. The results from NASA Supercritical Airfoil 9a and NACA 63-415 are omitted as our assumption that the $c_{d,p} \approx c_d$ do not hold. As the only available measurements are from wake rakes that measure the total drag, it is difficult to validate the drag predictions from our model for these two cases. For the Supercritical Airfoil 9a, the operating

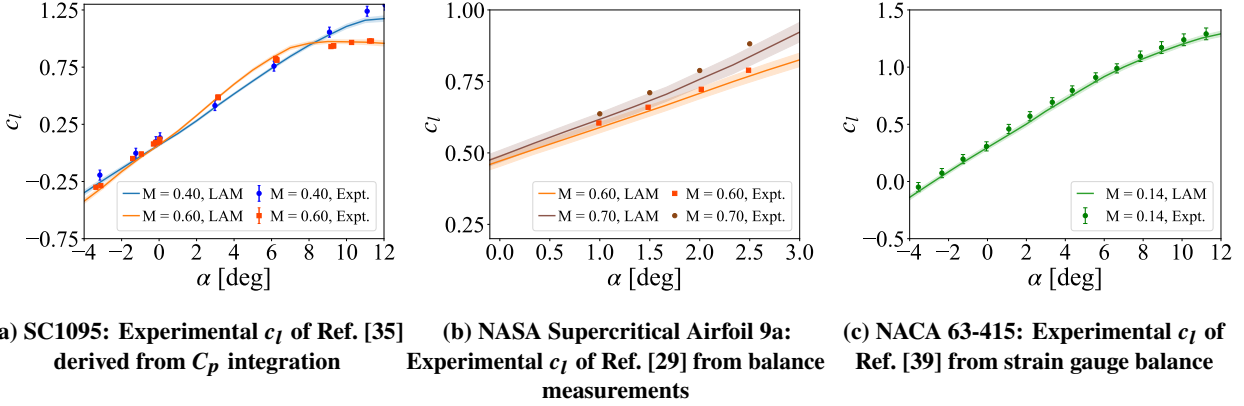


Fig. 17 Predicted c_l at various angles of attack, freestream Mach numbers, and airfoils. The error bars represent two standard deviations.

conditions of the test data are at near-zero angles of attack. At the low values of α , skin friction drag can make up a greater portion of the total drag [45]. Supercritical airfoils are optimized for minimal pressure drag at high M compared to conventional airfoils, which deviates from our assumption even further. As for the NACA 63-415, the experimental conditions are at a much lower freestream Mach number than the SC1095, which corresponds to a relatively higher skin friction drag. Thus, significant underprediction would be expected for these airfoils when using our method to calculate c_d . For the SC1095, where the assumption of a dominant pressure drag is valid, a good agreement can be seen. The maximum error (Δc_d) was found to be 0.018 at $\alpha = 6^\circ$ for one of the measurements. However, a second measurement at the same operating condition has a much lower error of 0.005.

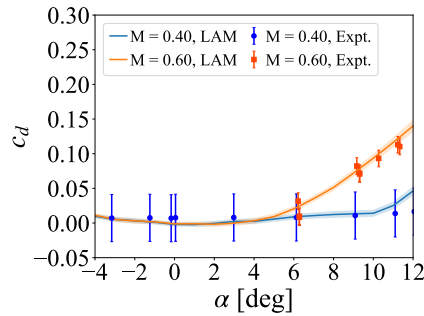


Fig. 18 Predicted c_d at various angles of attack and freestream Mach numbers for SC1095. The error bars represent two standard deviations. Experimental c_d are wake rake measurements from Ref. [29].

In Fig. 19, the predicted c_m is compared against the measurements. The predictions are found to be accurate as well. For example, Fig. 19a shows that the the increase in the pitching moment magnitude of SC1095 with increasing α is captured especially well. Figures 19b and 19c also show that the experimental measurements fall within or is close to the 95% confidence interval. The greatest value of Δc_m was found to be approximately 0.01.

The presented figures demonstrate that the proposed method effectively predicts the aerodynamic force coefficients,

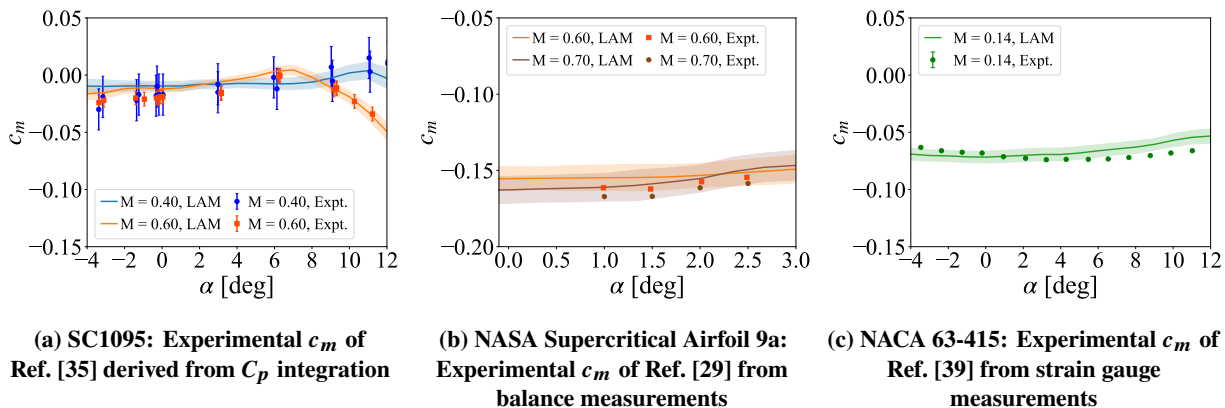


Fig. 19 Predicted c_m at various angles of attack, freestream Mach numbers, and airfoils. The error bars represent two standard deviations.

with the predictions generally correlating well with experimental measurements. The trends in lift, drag, and moment coefficients match the expected behavior of the airfoils across different freestream Mach numbers and angles of attack. Overall, the model shows promise as a comprehensive aerodynamic analysis of an airfoil, when applied under conditions where the assumptions hold.

C. Beyond the Training Data

As discussed in Sec. III.C, the model demonstrates the highest accuracy when making predictions within the range of the training data. In the case of the LAM, this range corresponds to $-4.0^\circ \leq \alpha \leq 12.0^\circ$ and $0.0 \leq M \leq 0.75$. Recognizing the model’s limitation and its reduction of performance beyond the training data is particularly valuable for users, as it facilitates informed decision-making about the appropriate use of the tool.

Figure 20 illustrates the model’s performance beyond the training data. For a SC1095 airfoil, the C_p is predicted for high values of angles of attack and freestream Mach numbers not included in the training range. It is evident that, in this region, the unreliability is marked by a substantial increase in the posterior uncertainties. With further deviation from the training data—such as an extremely high freestream Mach number ($M = 10.0$) or angle of attack ($\alpha = 90^\circ$)—the bias-variance trade-off becomes apparent, leading to a physically implausible mean C_p , such as a flat line.

D. Grid Resolution

Our model allows the C_p to be generated at an arbitrary set of locations. In contrast, results from CFD simulations depend on cell coordinates, and NN-based ML models typically produce outputs on pre-defined grids.

Figure 21 illustrates LAM’s capability to generate results on a very fine grid. The C_p distribution of a S809 airfoil at $\alpha = 5.13^\circ$ and $M = 0.15$ was predicted by the LAM and compared against results from a RANS simulation and CNN-based ML model presented by Hui et al [8]. The RANS simulation was run using SU2 [47] on a single processor with a C-grid mesh that consists of 65,845 points. The run was considered converged when the variations in c_l and c_d

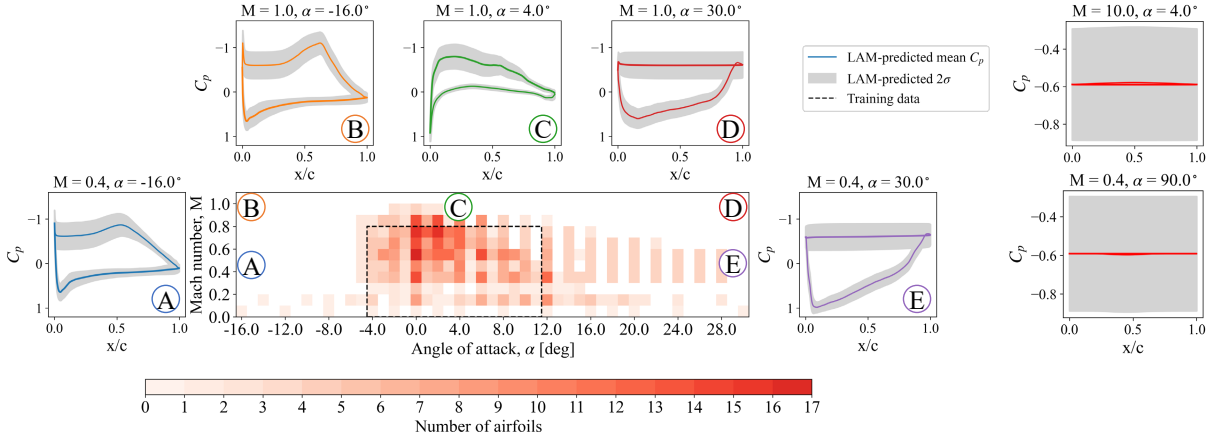


Fig. 20 Predictions of C_p and two standard deviations for SC1095 under operating conditions beyond the training data. The extent of the training data in α and M is highlighted by the black dotted box.

fell below 1×10^{-5} . It can be seen from the figure that the LAM has the finest resolution of points along the airfoil of 700 points, compared to 281 points of the SU2 simulation and 98 points of the CNN model. Moreover, increasing the resolution of the model is trivial, requiring only a change in the size of the input matrix.

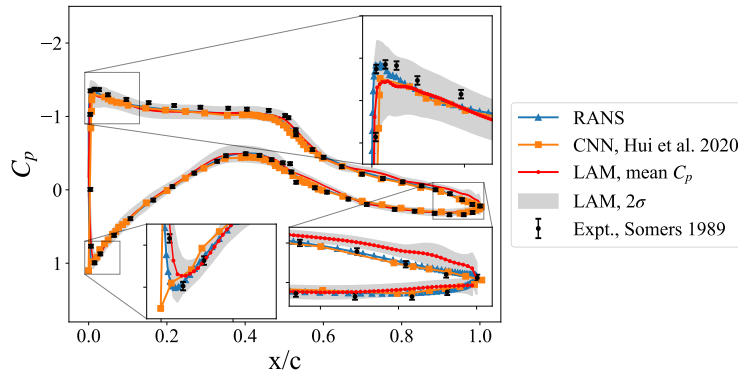


Fig. 21 Comparison of C_p predictions between RANS, CNN-based model, and LAM. Note the difference in grid resolution for each model. Experimental measurements are from Ref [48].

E. Computational Performance and Capability

Lastly, the computational cost and accuracy of LAM are compared against two physics-based solvers: RANS (SU2) and XFOIL [49], as shown in Table 1. The comparison was performed for S809 at $\alpha = 5.13^\circ$ and $M = 0.15$ (Sec. IV.D) and NACA 0012 at $\alpha = 1.89^\circ$ and $M = 0.70$. The mesh for NACA 0012 was obtained from the SU2 tutorial repository and consists of 229,336 grid points. The numerical simulation was conducted at $\alpha = 1.50^\circ$, which was the angle that best matched the experimental validation data as determined in Ref. [50]. As with the S809 case, the convergence criteria were $\Delta c_l, \Delta c_d \leq 1 \times 10^{-5}$. XFOIL results were obtained with 494 panels, the highest resolution possible in the program. It should be noted that while both airfoils were included in the train sets, the operating conditions were not.

Solver	Case	Wall Clock Time	MAE _{enclosed}	MAE	Compressibility	Separation
RANS (SU2)	S809	1349.76s	0.028	0.055		
	NACA 0012	1021.20s	0.016	0.034	✓	✓
LAM	S809	CPU: 5.81s / GPU: 1.55s	0.030	0.056	✓	✓
	NACA 0012	CPU: 5.78s / GPU: 1.79s	0.036	0.042	✓	✓
XFOIL	S809	1.98s	0.030	0.052	×	×
	NACA 0012	2.08s	0.071	0.100	×	×

Table 1 Computational efficiency and capabilities of different types of airfoil aerodynamic tools. All cases were run with a single processor CPU, except for the LAM GPU case, which was run on one NVIDIA A100 GPU.

Figure 22 shows the comparison between the predicted C_p distributions. RANS simulations model the governing equations of fluid dynamics, which allows for accurate capturing of airfoil physics. This is reflected by the lowest error overall, in both MAE_{enclosed} and MAE. However, it consumes the highest wall clock time and requires the user’s technical skills such as meshing techniques and turbulence modeling decisions.

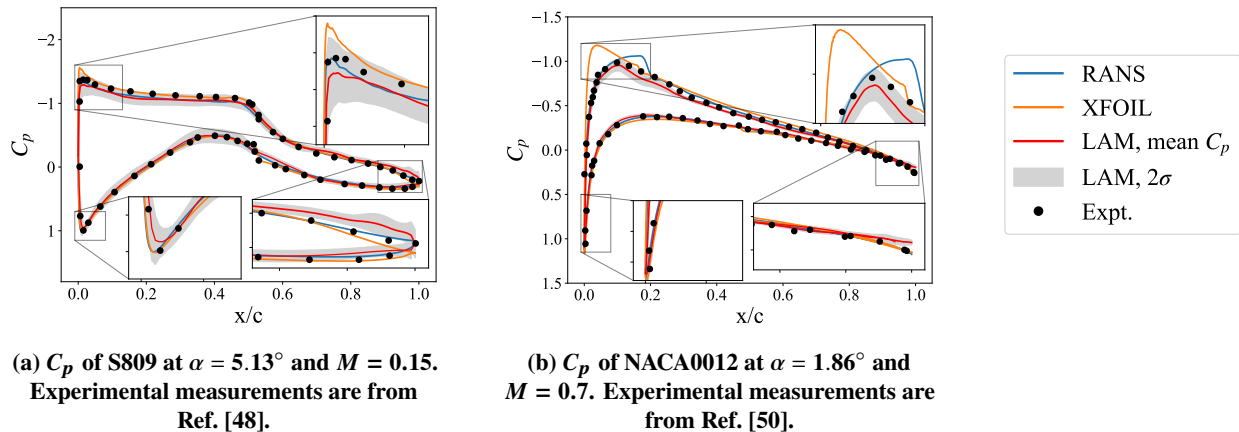


Fig. 22 Comparison of predicted C_p for different aerodynamic solvers: RANS simulations, LAM, and XFOIL.

The S809 case is in the incompressible regime. One notable feature of the C_p curve is the drop in pressure that occurs at mid-chord, which is caused by boundary layer transition. In this case, XFOIL was found to yield accurate results, on-par with CFD, with a low computational cost of 1.98 seconds. It should be noted that precisely modeling transition behavior requires controlling parameters such as the critical amplification factor (N_{crit}) and transition locations, which requires user experience with software. As a potential flow solver, XFOIL cannot resolve complex aerodynamics such as compressibility effects and flow separation. This is noticeable in the NACA 0012 case at $M = 0.70$, where there is significant mismatch in C_p at the suction peak, and an increase in the errors.

In contrast, LAM has a significantly reduced runtime compared to that of RANS, and even outperforms XFOIL when utilizing a GPU. The model yields a similar accuracy to that of XFOIL at low freestream M , and successfully captures the boundary layer transition with no user input on transition modeling. Furthermore, the model also captures

compressibility effects as demonstrated in the NACA 0012 case.

V. Conclusion

In this study, the development of a Large Airfoil Model (LAM) was presented, also accessible on <https://large-airfoil-model.azurewebsites.net>. The proposed machine learning model, will be able to answer complex technical questions on aerodynamic characteristics of airfoils, which serve as building blocks in performing complex aerodynamic tasks (forward and inverse problems) for aircraft, rotorcraft, or wind turbine applications.

The first component of the model is the airfoil surface pressure information repository of experiments (ASPIRE), an openly available database of experimental measurements of airfoil pressure distributions. ASPIRE includes digitized wind tunnel experimental data for various airfoil families and applications such as general aviation, rotorcraft, and wind turbines. The continually expanding database covers a wide variety of operating conditions, ranging from -30° to 30° in α and 0.0 to 1.0 in freestream Mach number, M . The database contains 2802 unique pressure distributions from 68 airfoils. The goal is to continue expanding the database and fill in any gaps that exist in terms of airfoil families and years of publication. Contributions can be made on the aforementioned website.

We utilize the data made available from the digitization process to train a deep airfoil prediction tool (ADAPT), a deep kernel learning model. While we created a single general model to take advantage of the breadth of the data in ASPIRE, we note that it would also be possible to create multiple specialized models depending on the user's requirements. ADAPT, trained on experimental data as opposed to numerical simulations, offers a Bayesian means of pressure prediction. This allows the proper characterization of the uncertainties associated with experimental measurements and digitization. The model yielded a MAE_{enclosed} , the mean absolute error in the area enclosed by the pressure curves, of 0.029 on the test data and had good visual correlation.

As a natural consequence of the C_p predictions, the LAM predictions allowed for the calculation of aerodynamic force coefficients using a Monte Carlo approach. The results showed good correlations with the experimental lift, drag, and moment coefficients, c_l , c_d , and c_m , with the maximum errors of 0.05, 0.018, and 0.01, respectively.

Since ADAPT is fundamentally a Gaussian process model, the predictions can be performed at an arbitrary set of locations. This allows the model to yield C_p values at an infinite grid resolution, which provides greater flexibility than convolutional neural networks based airfoil aerodynamics models, which predict C_p on a preset grid.

Finally, the model was found to be computationally efficient, requiring an average of 5.80 seconds on a single CPU to generate predictions for a S809 at $M = 0.15$, $\alpha = 5.13^\circ$ and NACA 0012 at $M = 0.70$, $\alpha = 1.86^\circ$. When accelerated by a single A100 GPU, it outperformed XFOIL, a potential-flow based solver, with an average of 1.67 seconds. Unlike the low-fidelity method, the LAM has the capability to capture complex aerodynamic phenomena, such as compressibility effects, transition, and flow separation, having been trained on such effects. This means that the LAM does not require the user's expertise on specific software to model specific phenomena accurately.

Acknowledgments

The authors would like to thank Aaditya Hingoo, Ryan McKee, Tom Hoang, Bipin Koirala, and Grant Ewing for their assistance in the digitization of airfoil experimental data, and Chris Silva, Vengalattore Nagaraj, and Robert Scott for their guidance on key design questions.

This research was partially funded by the U.S. Government under Cooperative Agreement No. W911W6-21-2-0001. The U.S. Government is authorized to reproduce and distribute reprints for Government purposes notwithstanding any copyright notation thereon.

The views and conclusions contained in this document are those of the authors and should not be interpreted as representing the official policies or position, either expressed or implied, of the U.S. Army Combat Capabilities Development Command (DEVCOM), Aviation & Missile Center (AvMC), or the U.S. Government.

References

- [1] Brown, T., Mann, B., Ryder, N., Subbiah, M., Kaplan, J. D., Dhariwal, P., Neelakantan, A., Shyam, P., Sastry, G., Askell, A., Agarwal, S., Herbert-Voss, A., Krueger, G., Henighan, T., Child, R., Ramesh, A., Ziegler, D., Wu, J., Winter, C., Hesse, C., Chen, M., Sigler, E., Litwin, M., Gray, S., Chess, B., Clark, J., Berner, C., McCandlish, S., Radford, A., Sutskever, I., and Amodei, D., “Language Models are Few-Shot Learners,” *Advances in Neural Information Processing Systems*, Vol. 33, Curran Associates, Inc., 2020, pp. 1877–1901. <https://doi.org/10.48550/arXiv.2005.14165>.
- [2] Anthropic, “Introducing Claude,” <https://www.anthropic.com/news/introducing-claude>, 2023.
- [3] Anil, R., Borgeaud, S., Alayrac, J.-B., Yu, J., Soricut, R., Schalkwyk, J., Dai, A. M., Hauth, A., Millican, K., Silver, D., Johnson, M., Antonoglou, I., Schrittwieser, J., et al., “Gemini: A Family of Highly Capable Multimodal Models,” <https://arxiv.org/abs/2312.11805>, 2024. <https://doi.org/10.48550/arXiv.2312.11805>.
- [4] Thirunavukarasu, A. J., Ting, D. S. J., Elangovan, K., Gutierrez, L., Tan, T. F., and Ting, D. S. W., “Large language models in medicine,” *Nature Medicine*, Vol. 29, 2023, p. 1930–1940. <https://doi.org/10.1038/s41591-023-02448-8>.
- [5] Wang, L., Chou, J., Zhou, X., Tien, A., and Baumgartner, D. M., “AviationGPT: A Large Language Model for the Aviation Domain,” <https://arxiv.org/abs/2311.17686>, 2023.
- [6] Tikayat Ray, A., Pinon Fischer, O. J., Mavris, D. N., White, R. T., and Cole, B. F., “aeroBERT-NER: Named-Entity Recognition for Aerospace Requirements Engineering using BERT,” *AIAA SCITECH 2023 Forum*, 2023. <https://doi.org/10.2514/6.2023-2583>.
- [7] Yilmaz, E., and German, B., “A Convolutional Neural Network Approach to Training Predictors for Airfoil Performance,” *18th AIAA/ISSMO Multidisciplinary Analysis and Optimization Conference*, 2017. <https://doi.org/10.2514/6.2017-3660>.
- [8] Hui, X., Bai, J., Wang, H., and Zhang, Y., “Fast pressure distribution prediction of airfoils using deep learning,” *Aerospace Science and Technology*, Vol. 105, 2020, p. 105949. <https://doi.org/10.1016/j.ast.2020.105949>.

- [9] Zhang, H., “A novel deep-learning-based pressure distribution prediction approach of airfoils,” *Proceedings of the Institution of Mechanical Engineers, Part G: Journal of Aerospace Engineering*, Vol. 237, No. 16, 2023, pp. 3786–3799. <https://doi.org/10.1177/09544100231206570>.
- [10] Constantine, P. G., Dow, E., and Wang, Q., “Active Subspace Methods in Theory and Practice: Applications to Kriging Surfaces,” *SIAM Journal on Scientific Computing*, Vol. 36, No. 4, 2014, pp. A1500–A1524. <https://doi.org/10.1137/130916138>.
- [11] Grey, Z. J., and Constantine, P. G., “Active Subspaces of Airfoil Shape Parameterizations,” *AIAA Journal*, Vol. 56, No. 5, 2018, pp. 2003–2017. <https://doi.org/10.2514/1.J056054>.
- [12] Wong, C. Y., Seshadri, P., Scillitoe, A., Duncan, A. B., and Parks, G., “Blade Envelopes Part I: Concept and Methodology,” *Journal of Turbomachinery*, Vol. 144, No. 6, 2022, p. 061006. <https://doi.org/10.1115/1.4053239>.
- [13] Wong, C. Y., Seshadri, P., Parks, G. T., and Girolami, M., “Embedded ridge approximations,” *Computer Methods in Applied Mechanics and Engineering*, Vol. 372, 2020, p. 113383. <https://doi.org/10.1016/j.cma.2020.113383>.
- [14] Zhang, Y., Sung, W. J., and Mavris, D. N., “Application of Convolutional Neural Network to Predict Airfoil Lift Coefficient,” *2018 AIAA/ASCE/AHS/ASC Structures, Structural Dynamics, and Materials Conference*, 2018. <https://doi.org/10.2514/6.2018-1903>.
- [15] Liu, R.-L., Hua, Y., Zhou, Z.-F., Li, Y., Wu, W.-T., and Aubry, N., “Prediction and optimization of airfoil aerodynamic performance using deep neural network coupled Bayesian method,” *Physics of Fluids*, Vol. 34, No. 11, 2022, p. 117116. <https://doi.org/10.1063/5.0122595>.
- [16] Cornelius, J., and Schmitz, S., “Dragonfly Rotor Optimization using Machine Learning Applied to an OVERFLOW Generated Airfoil Database,” *Vertical Flight Society Forum 80*, 2024. <https://doi.org/10.4050/F-0080-2024-1316>.
- [17] Anhichem, M., Timme, S., Castagna, J., Peace, A., and Maina, M., “Bayesian Approaches for Efficient and Uncertainty-Aware Prediction of Pressure Distributions,” *AIAA SCITECH 2024 Forum*, 2024. <https://doi.org/10.2514/6.2024-0253>.
- [18] Anhichem, M., Timme, S., Castagna, J., Peace, A., and Maina, M., “Multifidelity Data Fusion Applied to Aircraft Wing Pressure Distribution,” *AIAA AVIATION 2022 Forum*, 2022. <https://doi.org/10.2514/6.2022-3526>.
- [19] Common Crawl Foundation, “Common Crawl,” <https://commoncrawl.org/>, 2007.
- [20] Gao, L., Biderman, S., Black, S., Golding, L., Hoppe, T., Foster, C., Phang, J., He, H., Thite, A., Nabeshima, N., Presser, S., and Leahy, C., “The Pile: An 800GB Dataset of Diverse Text for Language Modeling,” <https://arxiv.org/abs/2101.00027>, 2020.
- [21] Penedo, G., Malartic, Q., Hesslow, D., Cojocar, R., Cappelli, A., Alobeidli, H., Pannier, B., Almazrouei, E., and Launay, J., “The RefinedWeb Dataset for Falcon LLM: Outperforming Curated Corpora with Web Data, and Web Data Only,” <https://arxiv.org/abs/2306.01116>, 2023.
- [22] Spaid, F. W., Dahlin, J. A., Bachalo, W. D., and Stivers Jr., L. S., “An Experimental Study of Transonic Flow About a Supercritical Airfoil,” NASA TM-81336, 1983.

- [23] Chen, J., Wang, Q., Zhang, S., Eecen, P., and Grasso, F., “A new direct design method of wind turbine airfoils and wind tunnel experiment,” *Applied Mathematical Modelling*, Vol. 40, No. 3, 2016, pp. 2002–2014. <https://doi.org/10.1016/j.apm.2015.09.051>.
- [24] Ragni, D., Ferreira, C. S., and Correale, G., “Experimental investigation of an optimized airfoil for vertical-axis wind turbines,” *Wind Energy*, Vol. 18, No. 9, 2015, pp. 1629–1643. <https://doi.org/10.1002/we.1780>.
- [25] Saradhi, “ExtractTable,” <https://extracttable.com/>, 2024.
- [26] Johnson, P. J., “Pressure Distributions on the Blade Sections of the NACA 10-(3)(090)-03 Propeller under Operating Conditions,” NACA RM-L50A26, 1950.
- [27] Stanewsky, E., and Thibert, J. J., “Airfoil SKF 1.1 with Maneuver Flap,” AGARD-AR-138, 1979.
- [28] Ladson, L. C., Hill, S. A., and Johnson, J. G. W., “Pressure Distributions from High Reynolds Number Transonic Tests of an NACA 0012 Airfoil in the Langley 0.3-Meter Transonic Cryogenic Tunnel,” NASA TM-100526, 1987.
- [29] Harris, C. D., “Experimental Investigation of a 10 Percent Thick NASA Supercritical Airfoil Section,” AGARD-AR-138, 1979.
- [30] Pinkerton, R. M., “The Variation with Reynolds Number of Pressure Distribution over an Airfoil Section,” NACA TR-613, 1938.
- [31] Stivers Jr., L. S., “Effects of Subsonic Mach Number on the Forces and Pressure Distributions on Four NACA 64a-series Airfoil Sections at Angles of Attack as High as 28 Degrees,” NACA TN-162, 1985.
- [32] Johnson Jr., W. G., Hill, A. S., and Eichmann, O., “Pressure Distributions From High Reynolds Number Tests of a NASA SC(3)-0712(B) Airfoil in the Langely 0.3-Meter Transonic Cryogenic Tunnel,” NASA TM-86370, 1985.
- [33] Cook, P. H., McDonald, M. A., and Firmin, M. C. P., “Airfoil RAE 2822 - Pressure Distributions, and Boundary Layer and Wake Measurements,” AGARD-AR-138, 1979.
- [34] Rohatgi, A., “WebPlotDigitizer,” <https://automeris.io/WebPlotDigitizer.html>, 2024.
- [35] Flemming, R. J., “An Experimental Evaluation of Advanced Rotorcraft Airfoils in the NASA Ames Eleven-foot Transonic Wind Tunnel,” NASA CR-166587, 1984.
- [36] Thibert, J. J., Grandjacques, M., and Ohman, L. H., “NACA 0012 Airfoil,” AGARD-AR-138, 1979.
- [37] Leishman, G. J., *Principles of Helicopter Aerodynamics*, Cambridge University Press, 2006.
- [38] Wilson, A. G., Hu, Z., Salakhutdinov, R., and Xing, E. P., “Deep Kernel Learning,” *Proceedings of the 19th International Conference on Artificial Intelligence and Statistics*, Vol. 51, PMLR, Cadiz, Spain, 2016, pp. 370–378. <https://doi.org/10.48550/arXiv.1511.02222>.
- [39] Bak, C., Fuglsang, P., Johansen, J., and Antoniou, I., “Wind tunnel tests of the NACA 63-415 and a modified NACA 63-415 airfoil,” Risø-R-1193(EN), 2000.

- [40] Kingma, D. P., and Ba, J., “Adam: A Method for Stochastic Optimization,” <https://arxiv.org/abs/1412.6980>, 2017.
- [41] Izmailov, P., Podoprikin, D., Garipov, T., Vetrov, D., and Wilson, A., “Averaging weights leads to wider optima and better generalization,” *34th Conference on Uncertainty in Artificial Intelligence 2018, UAI 2018*, Association For Uncertainty in Artificial Intelligence (AUAI), 2018, pp. 876–885. <https://doi.org/10.48550/arXiv.1803.05407>.
- [42] Athiwaratkun, B., Finzi, M., Izmailov, P., and Wilson, A. G., “There Are Many Consistent Explanations of Unlabeled Data: Why You Should Average,” *International Conference on Learning Representations*, 2019. <https://doi.org/10.48550/arXiv.1806.05594>.
- [43] Hensman, J., Matthews, A., and Ghahramani, Z., “Scalable Variational Gaussian Process Classification,” *Proceedings of the Eighteenth International Conference on Artificial Intelligence and Statistics*, Vol. 38, PMLR, 2015, pp. 351–360. <https://doi.org/10.48550/arXiv.1411.2005>.
- [44] Titsias, M., “Variational Learning of Inducing Variables in Sparse Gaussian Processes,” *Proceedings of the Twelfth International Conference on Artificial Intelligence and Statistics*, Vol. 5, PMLR, 2009, pp. 567–574.
- [45] Anderson, J. D., *Fundamentals of Aerodynamics*, 5th ed., McGraw-Hill, 2011.
- [46] Montgomery, D. C., and Runger, G. C., *Applied Statistics and Probability for Engineers*, 7th ed., Wiley, 2018.
- [47] Economou, T. D., Palacios, F., Copeland, S. R., Lukaczyk, T. W., and Alonso, J. J., “SU2: An Open-Source Suite for Multiphysics Simulation and Design,” *AIAA Journal*, Vol. 54, No. 3, 2016, pp. 828–846. <https://doi.org/10.2514/1.J053813>.
- [48] Somers, D. M., “Design and Experimental Results for the S809 Airfoil,” NREL/SR-440-6918, 1997. <https://doi.org/10.2172/437668>.
- [49] Drela, M., “XFOIL,” <https://web.mit.edu/drela/Public/web/xfoil>, 2001.
- [50] Coakley, T., “Numerical simulation of viscous transonic airfoil flows,” *25th AIAA Aerospace Sciences Meeting*, 1987. <https://doi.org/10.2514/6.1987-416>.
- [51] Rasmussen, C. E., and Williams, C. K. I., *Gaussian Processes for Machine Learning*, The MIT Press, 2006. <https://doi.org/10.7551/mitpress/3206.001.0001>.
- [52] Stein, M. L., *Interpolation of Spatial Data*, Springer, 1999.
- [53] Grey, Z. J., Doronina, O. A., and Glaws, A., “Separable shape tensors for aerodynamic design,” *Journal of Computational Design and Engineering*, Vol. 10, No. 1, 2023, pp. 468–487. <https://doi.org/10.1093/jcde/qwac140>.

Appendix

A. Mathematical Preliminaries of Gaussian Process

First, let us assume the existence of a dataset \mathcal{D} which contains N input vectors related to airfoil geometry and operating conditions (i.e. the latent variables obtained from ADAPT's FCNN) and the corresponding pressure coefficient, C_p , at a given chordwise location; $(\mathbf{z}_n, y(\mathbf{z}_n))$ for $n = 1, \dots, N$. We assume that each observation of C_p is a noisy version of the underlying "true" value, $y_n = f(\mathbf{z}_n) + \epsilon_n$, where $\epsilon \sim \mathcal{N}(0, \sigma_n^2)$. The values of σ_n^2 of the likelihood model is obtained from the experimental accuracy recorded in ASPIRE. It will also be useful to assume that we require predictive pressure coefficient values at other locations. This training data and testing data is given by

$$\mathbf{Z} = \begin{bmatrix} \mathbf{z}_1 \\ \vdots \\ \mathbf{z}_N \end{bmatrix}, \mathbf{y} = \begin{bmatrix} y(\mathbf{z}_1) \\ \vdots \\ y(\mathbf{z}_N) \end{bmatrix} \text{ and } \mathbf{Z}^* = \begin{bmatrix} \mathbf{z}_1^* \\ \vdots \\ \mathbf{z}_M^* \end{bmatrix}, \mathbf{f}^* = \begin{bmatrix} f^*(\mathbf{z}_1) \\ \vdots \\ f^*(\mathbf{z}_M) \end{bmatrix}, \quad (10)$$

where the asterisk indicates the testing locations. In GP regression, we model the target variable as a Gaussian process, which is fully characterized by its mean function ($\mu(\mathbf{z})$) and covariance function ($k(\mathbf{z}, \mathbf{z}')$). The GP regression model can be defined as

$$f(\mathbf{z}) \sim \mathcal{GP}(\mu(\mathbf{z}), k(\mathbf{z}, \mathbf{z}')). \quad (11)$$

Then, the joint density of the observed data and the latent, noise-free function on the test points is given by

$$\begin{pmatrix} \mathbf{y} \\ \mathbf{f}_* \end{pmatrix} \sim \mathcal{N} \left(\begin{pmatrix} \mu_{\mathbf{Z}} \\ \mu_* \end{pmatrix}, \begin{pmatrix} \mathbf{K}_{\mathbf{Z},\mathbf{Z}} + \sigma_n^2 \mathbf{I} & \mathbf{K}_{\mathbf{Z},*} \\ \mathbf{K}_{\mathbf{Z},*}^T & \mathbf{K}_{*,*} \end{pmatrix} \right). \quad (12)$$

$\mathbf{K}_{\cdot,\cdot}$ denotes the covariance matrix between the GPs evaluated at either \mathbf{Z} or \mathbf{Z}^* . For example, $\mathbf{K}_{\mathbf{Z},\mathbf{Z}}$ represents the $N \times N$ covariance matrix between the GP at training data \mathbf{Z} while $\mathbf{K}_{\mathbf{Z},*}$ represents the $N \times M$ covariance matrix between the GP at the training data \mathbf{Z} and a set of test points \mathbf{Z}^* .

Given the training data of input-output pairs (\mathbf{Z}, \mathbf{y}) , the posterior Gaussian distribution at \mathbf{Z}_* can be written as

$$\mu_{*|\mathbf{Z}} = \mathbf{K}_{\mathbf{Z},*}^T (\mathbf{K}_{\mathbf{Z},\mathbf{Z}} + \sigma_y^2 \mathbf{I})^{-1} \mathbf{y} \text{ and} \quad (13)$$

$$\Sigma_{*|\mathbf{Z}} = \mathbf{K}_{*,*} - \mathbf{K}_{\mathbf{Z},*}^T (\mathbf{K}_{\mathbf{Z},\mathbf{Z}} + \sigma_y^2 \mathbf{I})^{-1} \mathbf{K}_{\mathbf{Z},*}. \quad (14)$$

Due to numerical instability that may arise from directly calculating the inverse $(\mathbf{K}_{\mathbf{Z},\mathbf{Z}} + \sigma_n^2 \mathbf{I})^{-1}$, a Cholesky decomposition

is performed where, $\mathbf{K}_\sigma = \mathbf{L}\mathbf{L}^T$. This allows the rewriting of Equations 13 and 14 as

$$\mu_{*|Z} = \mathbf{K}_{Z,*}^T \alpha, \text{ and} \quad (15)$$

$$\Sigma_{*|Z} = \mathbf{K}_{*,*} - \mathbf{v}^T \mathbf{v}, \quad (16)$$

where $\alpha = \mathbf{L}^T \backslash (\mathbf{L} \mathbf{y})$ and $\mathbf{v} = \mathbf{L} \backslash \mathbf{K}_{Z,*}$.

B. Kernel Function

As observed in the previous equations, the covariance function (also known as the kernel function) is a crucial ingredient in a Gaussian process regression, as it encodes our assumptions about the function which we wish to learn [51]. One of the most widely used kernel function is the Squared Exponential (SE) kernel, also known as the Radial Basis Function (RBF) kernel. The function is of the form

$$k_{SE}(\mathbf{z}, \mathbf{z}') = \sigma_f^2 \exp\left(-\frac{1}{2l^2} \|\mathbf{z} - \mathbf{z}'\|^2\right), \quad (17)$$

where the hyperparameter σ_f^2 denotes the kernel amplitude (or variance) and l denotes the length scale. One property of the SE kernel is that it is infinitely differentiable, which means that any GP employing this covariance function has mean square derivatives of all orders. Consequently, the model outputs have strong smoothness. This property of the SE kernel can prove detrimental in modeling some physical phenomena [52].

A commonly used alternative to the SE kernel is the Matérn class of covariance functions. The class includes a smoothness parameter, often denoted by ν , which allows the user to control the smoothness of the resulting GP sample paths. The parameter allows the function to perform better in modeling processes with discontinuities or sharp changes. The covariance is given by

$$k_{\text{Matérn}}(\mathbf{z}, \mathbf{z}') = \sigma_f^2 \frac{2^{1-\nu}}{\Gamma(\nu)} \left(\frac{\sqrt{2\nu} \|\mathbf{z} - \mathbf{z}'\|}{l}\right)^\nu K_\nu\left(\frac{\sqrt{2\nu} \|\mathbf{z} - \mathbf{z}'\|}{l}\right) \quad (18)$$

where Γ is the gamma function and K_ν is the modified Bessel function of the second kind. The most commonly used cases of the Matérn classes in machine learning are those where ν is a non-negative half-integers [51], namely $\nu = 1/2, 3/2$, and $5/2$. In this work, we use $\nu = 5/2$, which simplifies Eq. 18 to

$$k_{\nu=5/2}(\mathbf{z}, \mathbf{z}') = \sigma_f^2 \left(1 + \frac{\sqrt{5}}{l} \|\mathbf{z} - \mathbf{z}'\| + \frac{5}{3l^2} \|\mathbf{z} - \mathbf{z}'\|^2\right) \exp\left(-\frac{\sqrt{5}}{l} \|\mathbf{z} - \mathbf{z}'\|\right). \quad (19)$$

With the Matérn 5/2 kernel function, the Gaussian Process $f(\mathbf{z})$ is twice differentiable in the mean-square sense. This allows the model to capture the rapid changes in the pressure curves, often occurring at the suction peak or shocks,

while maintaining some level of smoothness.

C. Training Objectives

Training the model involves finding optimal values of the weights and biases of the fully connected network and GP hyperparameters \mathbf{t} (σ_f^2 and l^2), which are obtained by maximizing the marginal likelihood given the training targets \mathbf{y} :

$$\log p(\mathbf{y}|\mathbf{Z}, \mathbf{t}) = -\frac{1}{2}\mathbf{y}^T (\mathbf{K}_{Z,Z} + \sigma_n^2 \mathbf{I})^{-1} \mathbf{y} - \frac{1}{2} \log |\mathbf{K}_{Z,Z} + \sigma_n^2 \mathbf{I}| - \frac{N}{2} \log(2\pi), \quad (20)$$

where N is the number of training data, $\mathbf{K}_{Z,Z}$ represents the $N \times N$ covariance matrix between the GP at training data \mathbf{Z} , and σ_n^2 is the reported variance of the training data.

It is also worth emphasizing all hyperparameters, that we *jointly* learn all deep kernel hyperparameters, weights of the neural network (\mathbf{w}) and the parameters of the base kernel (\mathbf{t}), in an end-to-end fashion. The approach allows the incorporation of all components of the DKL process into a single model.

D. Analysis of Model Active Space

The LAM predicts an airfoil’s pressure distribution by first projecting the input data into a 10-dimensional latent space and then mapping these latent variables to an output multivariate normal distribution as a Gaussian process. In this section of the Appendix, we analyze the model’s behavior in this active space, which is important for ensuring that the model operates with a robust and interpretable parameterization [53]. Dimensionality reduction, the process of simplifying the data while preserving its essential structure, plays a key role in this analysis.

In many studies, Principal Component Analysis (PCA) is the preferred technique for improving the interpretability of the active space. The method decomposes a data matrix \mathbf{Z} into $\mathbf{Z} = \mathbf{U}\mathbf{\Sigma}\mathbf{V}^T$ where \mathbf{U} is the matrix of left singular vectors, $\mathbf{\Sigma}$ is the diagonal matrix of singular values, and \mathbf{V} is the matrix of right singular vectors. The decomposition allows for the identification of the principal components, the directions in the data that exhibit the most variance.

However, real-world data is often represented through noisy measurements, including the digitized data in ASPIRE. The presence of noise can significantly alter the principal component directions. Therefore, in this work, Robust Principal Component Analysis (RPCA) is employed as opposed to the standard PCA. RPCA is an optimization strategy where a data matrix is decomposed into a low-rank component and a sparse component, effectively separating the underlying data structure from the outliers.

Mathematically, RPCA solves the following optimization problem:

$$\min_{\mathbf{L}, \mathbf{S}} \|\mathbf{L}\|_* + \lambda \|\mathbf{S}\|_1 \quad \text{subject to} \quad \mathbf{Z} = \mathbf{L} + \mathbf{S}, \quad (21)$$

where \mathbf{L} is the low-rank component, \mathbf{S} is the sparse component, $\|\mathbf{L}\|_*$ denotes the sum of singular values of \mathbf{L} , and $\|\mathbf{S}\|_1$

denotes the L_1 norm of \mathbf{S} . The parameter λ balances the trade-off between the low-rank approximation and the sparsity of the outliers. When λ is set to a high value, the influence of \mathbf{S} is minimized, and \mathbf{L} dominates the decomposition. In this case, the decomposition closely resembles that of standard PCA. Once the decomposition is achieved, \mathbf{L} is subjected to standard PCA procedure to obtain the principal components. These components, denoted as L_s , serve as the primary directions that capture the most variance in the cleaned, low-rank data.

In this investigation, an artificial test dataset was generated, consisting of all airfoils from the training set. The operating conditions ranged from $-4.0^\circ \leq \alpha \leq 12.0^\circ$ and $M = 0.30, 0.60, 0.70$. To better understand the overall behavior of the airfoils, c_l was studied instead of individual C_p values. The process required the generation of 601 points along the entire airfoil for each α - M pair. The artificial test set was fed into the deep neural network which produces the 10 latent variables, resulting in a matrix \mathbf{Z} of size $1,060,164 \times 10$. The same integral operator used to calculate c_l was then applied to this matrix. The final $1,764 \times 10$ array of integrated latent variables was processed through RPCA to obtain \mathbf{L} . From the cumulative explained variance by individual L components (Fig. 23), it was found that 3 components were sufficient to explain approximately 95% of the variance. This allowed us to analyze contributions of all variables using the $1,764 \times 3$ matrix, which conveniently could be visualized in a 3D plot.

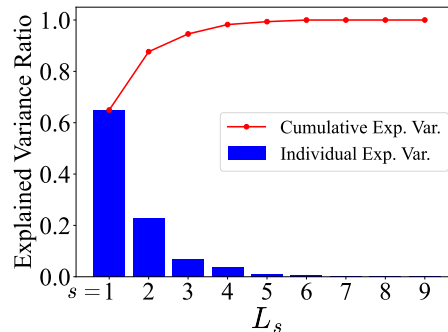
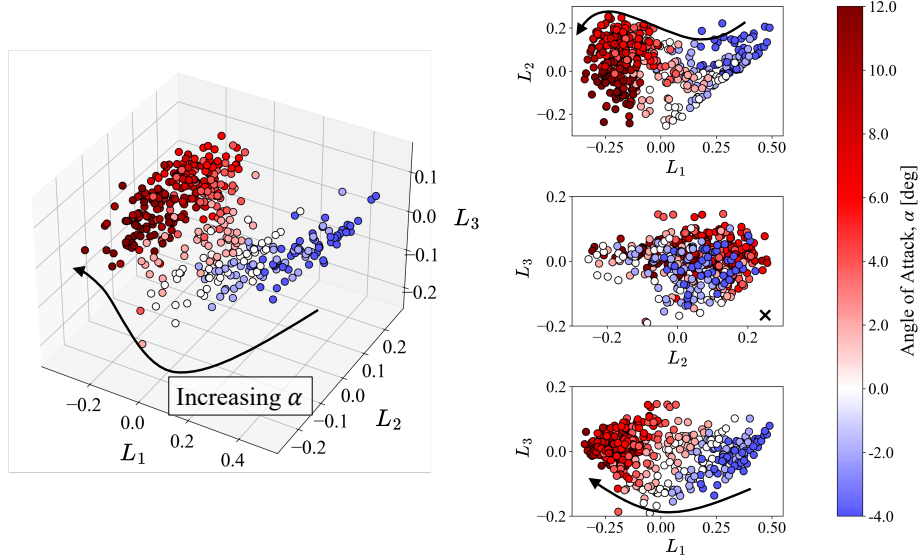


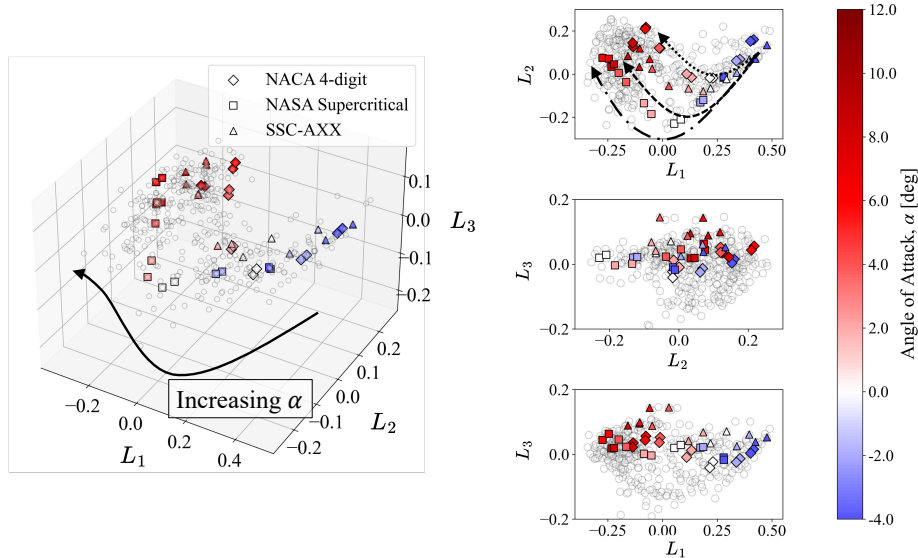
Fig. 23 Individual and cumulative explained variances of the integrated latent variables

Figure 24 depicts the distribution of the latent variables within the active space, where each point is colored by its angle of attack. A clear trajectory with respect to α can be observed. The trend is clearest in the L_1 - L_2 plane, where increasing α in the pre-stall regime corresponds to a parabolic path in the plane. The latent variables deviate from this crescent curve as the angle of attack approaches stall. At $\alpha = 12^\circ$, it can be seen that the latent variables decrease along L_2 with relatively smaller changes in the L_1 direction.

Figure 24b shows 3 airfoil families in isolation in the same active space at $M = 0.70$. NACA 4-digit series, NASA Supercritical airfoils, and SSC-AXX airfoils were chosen as they were designed for different purposes and thus exhibit different behaviors with respect to α and M . For instance, the 3 airfoil families have different degrees of camber and airfoil thicknesses. Consequently, with changing α and a fixed $M = 0.70$, we observe that the 3 airfoil families follow distinct trajectories. This is most noticeable in the L_1 - L_2 plane, where NASA Supercritical airfoil follows the



(a) Distribution of the latent variables within the active space, colored by α



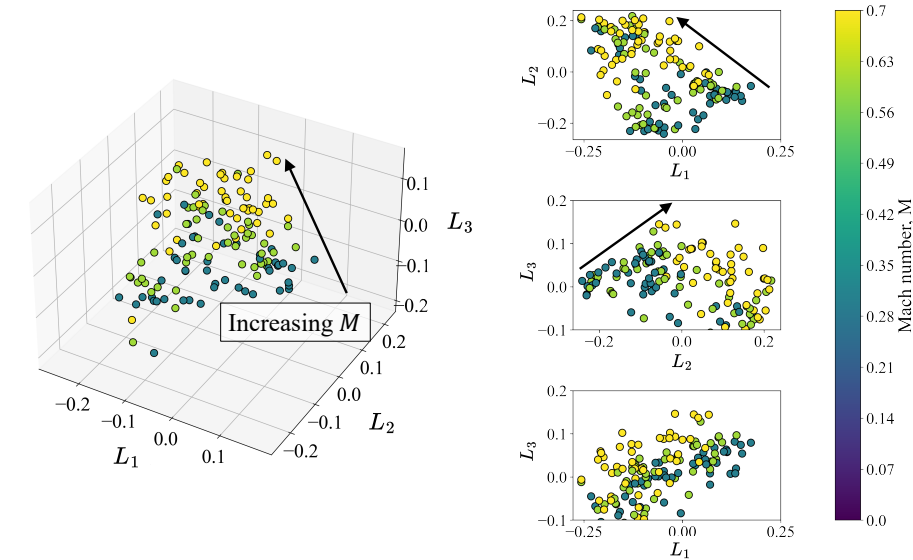
(b) Trajectories followed by NACA 4-digit, NASA Supercritical and SSC-AXX families in response to changing α

Fig. 24 Analysis of the model active space with varying α and $M = 0.70$

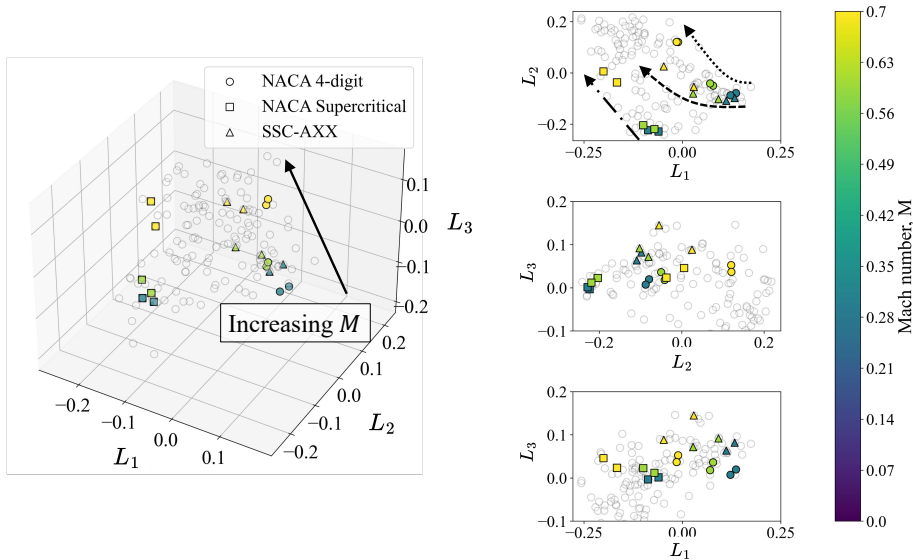
outermost, SSC-AXX the middle, and NACA 4-digit series the innermost trajectories respectively.

The behavior of the latent variables with respect to varying freestream Mach numbers is shown in Fig. 25. With increasing M , we see a decrease in the L_1 direction, and an increase in L_2 and L_3 directions. The identified trends are less distinct than those in relation to α . This is likely due to the fact that angle of attack, in general, has a greater impact on c_l compared to the freestream Mach number. In Fig. 25b, the 3 separate trajectories are followed by different airfoil families. NASA Supercritical airfoil follows the outermost, and NACA 4-digit series the innermost diagonal paths. The SSC-AXX family follows a path between these two airfoil families. As with Fig. 24b, the clearly discernible trajectories

are due to the fact that the airfoils are optimized for different freestream Mach number regimes. NACA 4-digit series airfoils were designed for incompressible flows and NASA Supercritical airfoils for transonic regimes. SSC-AXX airfoils, on the other hand, is a rotorcraft airfoil which must perform well in a wide range of freestream Mach numbers.



(a) Distribution of the latent variables within the active space, colored by M



(b) Trajectories followed by NACA 4-digit, NASA Supercritical and SSC-AXX families in response to changing M

Fig. 25 Analysis of the model active space with varying M and $\alpha = 4.0^\circ$

The analysis of the active space learned by ADAPT's deep neural network showed that the latent variables are grouped into distinct clusters in terms of α and M . While the overall behavior remains similar, the trajectories taken by an airfoil within the active space differs based on the airfoil family. The results serve as the evidence that the model has captured an interpretable and physical mapping between the input space and the latent space during training.